

A BEM/FEM Coupling Approach for Fluid-Structure Interaction Simulation of Cell Motion

S. Y. Wang¹, P. Q. Chen¹, K. M. Lim^{1,2,*} and B. C. Khoo^{1,2}

¹ Singapore-MIT Alliance, E4-04-10, 4 Engineering Drive 3, Singapore 117576.

² Department of Mechanical Engineering, National University of Singapore, Singapore 119260.

Received 4 February 2009; Accepted (in revised version) 22 September 2009

Communicated by Yao Zheng

Available online 6 January 2010

Abstract. In this paper, accurate and efficient simulation of cell motion in a biological fluid flow is investigated. The membrane of a moving cell is represented by a thin shell composed of incompressible neo-Hookean elastic materials and the liquids around the membrane are approximated as incompressible Newtonian flows with low Reynolds numbers. The biofluid mechanics is approximated by the Stokes flow equations. A low-order BEM model is developed for the two biological fluids coupled at the membrane surface. The moving boundary problem in fluid mechanics can be effectively solved using the BEM with a GMRES solver. The FEM model based on a flat thin shell element is further developed to predict the membrane load due to the large deformation of a moving cell. Computational efficiency is greatly improved due to the one-dimensional reduction in the present BEM and FEM models. The BEM solver for the biological fluids is coupled with the FEM solver for the cell membrane at the membrane surface. The position of the membrane surface nodes is advanced in time by using the classical fourth-order Runge-Kutta method. Numerical instability is avoided by using a relatively small time step. Further numerical instabilities in the FEM solver is alleviated by using various techniques. The present method is applied to the FSI problems of cell motion in a cylindrical flow. Numerical examples can illustrate the distinct accuracy, efficiency and robustness of the present method. Furthermore, the importance of bending stiffness of a cell membrane for stable cell motion simulation is emphasized. It is suggested that the present approach be an appealing alternative for simulating the fluid-structure interaction of moving cells.

AMS subject classifications: 74K25, 74S15, 74S05, 74F10

PACS: 02.70.Dh, 02.30.Rz, 46.70.De, 83.10.-y

Key words: Fluid-structure interaction, coupling approach, boundary element method, finite element method, stability, thin shell element.

*Corresponding author. *Email addresses:* ShengYin.Wang@keppelom.com (S. Y. Wang), chpq2000@gmail.com (P. Q. Chen), limkm@nus.edu.sg (K. M. Lim), mpekbc@nus.edu.sg (B. C. Khoo)

1 Introduction

The motion of living cells in large vessels, narrow tubes, and microcapillaries is one of the most important physiological phenomena of biological systems. As a common type of living cells in the blood vessels, red blood cells, which consist of a nearly-Newtonian cytoplasm enclosed by a lipid bilayer and a supportive cytoskeleton network of proteins, are the vertebrate body's principal means of delivering oxygen from the lungs or gills to body tissues via the blood. Living cells can be generally modelled as capsules in the context of particulate microhydrodynamics [1–4], different from droplets and bubbles whose interfacial forces result from surface tension [5]. Various types of capsules exist in the fields of medicine, physiology, biotechnology, as well as in the pharmaceutical industry, with important applications in drug delivery and cell therapy [4].

In the process of cell motion, fluid-structure interaction (FSI) can be of significant importance due to the deformability of living cells [6]. The hydrodynamics inside and around the cell should be coupled with the membrane dynamics of the cell in a physiologically accurate manner. The fluid mechanics was usually approximately described by Newtonian low-Reynolds-number hydrodynamics [3–5,7]. The structural mechanics of cell membranes can be described by either the continuum thin-shell theories [1,4,8–12] or discrete molecular dynamics [13,14]. Despite less insight into the detailed molecular mechanical behaviors, the continuum approach using the thin-shell theories is easier to implement and more straightforward to use if only the biomechanical response at the cell level is needed [15]. The continuum approach can further assist in the development of more accurate molecular models since it can provide the forces to the cytoskeletal and subcellular components by appropriate distribution and transmission of the stresses induced on the cell. In this study, only the continuum approach using a thin-shell theory for the cell membrane simulation is considered. As noted in [16–19], the fluid-structure interactions are among the most important but challenging multiphysics problems with respect to both modeling and computational issues.

Tremendous research efforts have been devoted to the development of modeling and simulation approaches for the FSI problems of cell motion [4,18]. In the early efforts by Secomb [20,21], pellets consisting of an elastic solid were used to model the cells to illuminate some basic reviews in the context of biofluid dynamics. The fluid-structure interactions to describe the motion of individual cells were neglected. In order that the virtual incompressibility and elastic properties of the cell membrane can be taken into consideration, more accurate models using thin-shell theories were further developed [1,4,8–12]. Zarda et al. [8] are among the first researchers to use the finite element method (FEM) to solve the equations of low-Reynolds-number hydrodynamics around a steadily translating cell in a perfectly axisymmetric configuration. A membrane model with a finite dilation modulus and resistance to bending stresses was used, and axisymmetric flow through capillaries using the finite element method simulated. More realistic model for tightly-fitting cells based on the lubrication approximation was proposed by Secomb and co-workers [2,22–26]. A boundary-value problem involving ordinary differential equa-

tions was formulated, the effect of the endothelial surface layer was accounted for, lubrication analysis for three-dimensional (3D) flow was developed, and non-axisymmetric motion of tightly-fitting cells accounting for the effect of membrane tank-treading motion [4] was studied. As a more general pursuit, Barthès-Biesel and co-workers [27–29] studied the axisymmetric passage of capsules with spherical and spheroidal unstressed shapes through pores, tubes, and constrictions. Zhou and Pozrikidis [30] used the boundary element method (BEM) with interfacial tension based on surface tension with an incompressibility constraint as a model of the membrane. Local area conservation was enforced through a kinematic condition by ignoring the extensional properties of the membrane. Eggleton and Popel [1] used the immersed boundary method [31] to simulate capsule deformation in which internal and external fluid properties were equal. The methodology developed by Unverdi and Tryggvason [32] was adopted for tracking the interface and accounting for the changes in fluid properties. Front tracking requires the solution of Poisson's equation on the entire fluid grid at every time step, and can thus be computationally expansive to implement. To achieve the computational efficiency due to the one-dimension reduction, Pozrikidis [4] presented BEM-based numerical solutions for cells with spherical, oblate ellipsoidal, and biconcave unstressed shapes whose minimum distance from the tube wall is comparable to the tube radius. The cell membrane was assumed to obey a neo-Hookean constitutive equation that accounts for elastic response in shearing deformation without explicit resistance to surface dilatation and bending deformation. The simulations illustrated the significance of the cell deformability and demonstrated the effect of the cell shapes on the reduced convection velocity or hematocrit ratio and on the suspension apparent viscosity. Nevertheless, simulations with this theoretical model can result in shapes with cusps due to the local buckling at the trailing edge of the cell due to the lack of bending stiffness [1,4,19]. In the research work of [33], the boundary element method was applied to the computation of Stokes flow due to the motion or presence of a rigid particle in a fluid-filled tube with arbitrary geometry and the emphasis was put on the induced upstream to downstream pressure change to ameliorates the effect of domain truncation. Furthermore, Pozrikidis [34] investigated the axisymmetric motion of a periodic file of red blood cells through a circular capillary for arbitrary cell separations and tube diameters spanning a broad range. The mathematical formulation has taken into consideration the nearly incompressible and elastic properties of the cell membranes with respect to shearing and bending deformation from the unstressed shape of the biconcave disk. The problem was formulated and solved using the boundary integral method for axisymmetric Stokes flow, combined with the theory of axisymmetric thin shells to describe the membrane mechanics. The significance of the capillary radius and cell spacing on the discharge hematocrit and apparent viscosity of the one-dimensional suspension was illustrated, and the predictions of the lubrication flow model applicable for tightly-fitting cells [25] was validated. More recently, Liu et al. [18] applied the immersed finite element method to the modeling of biological systems including the transport of deformable cells. A Lagrangian FEM mesh for solids was devised to move on top of a background Eulerian FEM mesh for fluids to simplify the

mesh regeneration process. However, computational inaccuracy issue may arise since the distinct fluid-structure interface was smoothed and the continuity between the fluid and solid subdomains was enforced via the interpolation of the velocities and the distribution of the forces with an approximate delta function.

For solving the complicated FSI problems of cell motion in a real-world biological system, these modeling and simulation approaches may become computationally expansive and numerically unstable due to the inappropriate handling of several computational issues. Both the immersed boundary method [1, 31] and the immersed finite element method [18] need a 3D Eulerian fluid mesh which is at least sufficiently fine around the fluid-structure interface and the computational cost can thus be too high. The boundary element method developed by Pozrikidis [4] may pose a severe ill-conditioning problem since the system matrix is dense and unsymmetric, though one-dimension reduction can be achieved. The solution process may also be time consuming or even divergent. In simulating the membrane of a cell, the rigid body test was usually neglected. The finite element for the cell membrane was assumed to be free of any initial stresses or nodal forces before the external fluid loads were applied. However, large deformation due to both geometric and material nonlinearities may arise in cell motion and a finite element will be deformed and acted upon by a set of nodal forces that are in equilibrium at the beginning of each incremental step. Hence, the conventional patch test and eigenvalue test [35] for elements with no initial forces are not applicable. Without passing a rigid body test, the finite element may be disqualified for large deformation cell simulation. To time advance the cell membrane, a temporal integration at the fluid-structure interface was usually performed [1, 4, 18]. However, the explicit Euler's method in [4] requires a sufficiently small time step so that the computationally efficiency can be too low [4]. The semi-implicit method in [18] allows a relatively large time step, but the inconsistency between the applied forces and the membrane velocities may complicate the numerical analysis.

The objective of the present study is to present a robust FSI model for simulating the motion of deformable cells and capsules consisting of a Newtonian fluid and enclosed by an elastic membrane. The fluid mechanics for the internal and ambient fluids is represented by the 3D Stokes flow equations. The continuum structural mechanics for the cell membrane is described by the thin shell approximations. The significant difference between the present method and Pozrikidis [4] is the inclusion of the bending stiffness in cell membrane. This inclusion of the bending stiffness helps to alleviate the issue of buckling at the back of the cell. The classical fourth-order Runge-Kutta method is employed to perform the temporal integration to ensure the numerical accuracy. A FEM solver for the large deformation cell membrane is efficiently coupled with a BEM solver for the biological fluids. The present algorithm is applied to FSI problems of cell motion that have been investigated by previous researchers and improved accuracy, efficiency and robustness can be achieved.

2 Fluid-structure interaction simulation

2.1 Coupling approach

Fluid-structure interaction (FSI) is the interaction of a deformable or movable structure with an internal or ambient flow. Fluid-structural interaction problems have become one of the most important and challenging multiphysics problems regarding both modeling and computational issues [17]. In the FSI problems, both the fluid mechanics and the structural mechanics are involved and the whole reference domain Ω is composed of the fluid domain Ω^f and the structural domain Ω^s as

$$\begin{aligned}\Omega^f \cup \Omega^s &= \Omega, \\ \Omega^f \cap \Omega^s &= \Gamma^{\text{FSI}},\end{aligned}\quad (2.1)$$

where Γ^{FSI} is the fluid-structure interface. Fig. 1 displays a simple biological FSI problem of spherical cell motion in a circular cylinder, in which L is the truncation length and R the radius of the circular cylinder.

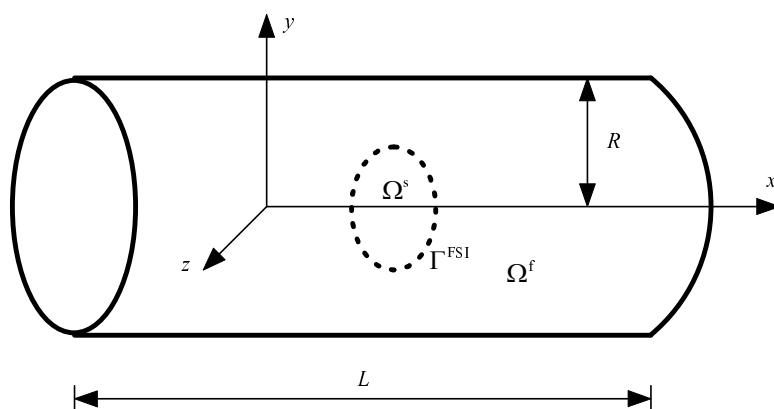


Figure 1: Cell motion in a circular cylinder.

In the fluid domain Ω^f , the fluid mechanics can be well described by Navier-Stokes equations under the incompressible flow assumption to simplify the flow analysis when dealing with liquids under steady conditions with small pressure changes, though all fluids are compressible in general. The well-known Navier-Stokes equations of incompressible flow of Newtonian fluids can be written as

$$\begin{aligned}\rho^f \left(\frac{\partial \mathbf{v}}{\partial t} + \mathbf{v} \cdot \nabla \mathbf{v} \right) &= -\nabla p + \mu \Delta \mathbf{v} + \mathbf{f}^f, \\ \text{div} \mathbf{v} &= 0,\end{aligned}\quad (2.2)$$

where t is time, ρ^f the fluid density, \mathbf{v} the fluid velocity vector, p the scalar pressure, μ the dynamic viscosity, and \mathbf{f}^f the fluid traction force vector exerted by the deformable

structure, which can be expressed as

$$\mathbf{f}^f(\mathbf{x}, t) = \int_{\Omega} \boldsymbol{\tau}^f(t) \delta(\mathbf{x}(t) - \mathbf{X}(t)) d\Omega, \quad (2.3)$$

in which \mathbf{x} is the time-independent position vector, $\boldsymbol{\tau}^f(t)$ the time-dependent traction force vector imposed by the structure at the fluid-structure interface Γ^{FSI} , $\mathbf{X}(t)$ the parameterized time-dependent fluid-structure interface.

In the structural domain Ω^s , the structural mechanics can be described by the following governing equation:

$$\rho^s \frac{d^2 \mathbf{u}}{dt^2} = \text{div} \boldsymbol{\sigma} + \mathbf{f}^s, \quad (2.4)$$

where ρ^s is the density of the structure, \mathbf{u} the structural displacement vector, $\boldsymbol{\sigma}$ the Cauchy stress tensor, and \mathbf{f}^s the traction force vector exerted by the fluid, which can be expressed as

$$\mathbf{f}^s(\mathbf{x}, t) = \int_{\Omega} \boldsymbol{\tau}^s(t) \delta(\mathbf{x}(t) - \mathbf{X}(t)) d\Omega, \quad (2.5)$$

in which $\boldsymbol{\tau}^s(t)$ is the time-dependent structural load vector imposed by the fluid at the fluid-structure interface Γ^{FSI} . According to Newton's third law, $\boldsymbol{\tau}^f(t)$ and $\boldsymbol{\tau}^s(t)$, as well as $\mathbf{f}^f(\mathbf{x}, t)$ and $\mathbf{f}^s(\mathbf{x}, t)$, are in pairs and must be equal in magnitude and opposite in direction.

The FSI problem described by Eqs. (2.1)-(2.5) can be numerically challenging due to the computational issues [17] and thus appropriate problem-dependent simplifications are desirable. For the biofluidic liquids (cytoplasm and plasma) inside and around a cell, as shown in Fig. 1, the fluid dynamics can be further approximated by the Newtonian low-Reynolds-number hydrodynamics. This approximation can be physiologically accurate for a class of living cells like the popular red blood cells [3-5, 7].

For the biofluidic liquids, if the Reynolds numbers are small enough, the inertial effects are insignificant and the motion of the liquids can be governed by the equations of Stokes flow [5, 36] given as follows:

$$\begin{aligned} -\nabla p + \mu \Delta \mathbf{v} + \mathbf{f}^f &= 0, \\ \text{div} \mathbf{v} &= 0. \end{aligned} \quad (2.6)$$

It should be noted that the Stokes flow approximation is appropriate in microcirculation since the Reynolds numbers are much less than unity [4]. Similarly, the structural governing equation in (2.4) can be simplified for the cell membrane as

$$\text{div} \boldsymbol{\sigma} + \mathbf{f}^s = 0. \quad (2.7)$$

Generally, the FSI problems can be solved by either a strong (tight, monolithic) or a weak (loose, partitioned) coupling approach, as detailed in [17, 37]. The strong coupling approach is based on the fully-coupled discretization of the governing equations and the resulting system of nonlinear algebraic equations may be solved by Newton's

method if good initial guesses for the solution are available [37, 38]. However, this approach is often labor intensive [17, 39] since the existing codes for fluid and structural solvers cannot be readily utilized and the programming modularity is thus poor. Moreover, the resulting system matrices can be severely ill-conditioned due to large number of unknowns involved and thus applications to large-scale FSI problems would become computationally prohibitive. On the other hand, the weak coupling approach [17] solves the complete FSI system by using an iterative strategy. The existing fluid and structural solvers are treated as black-box modules and coupled via a global fixed-point (Picard) iteration. During each iteration, a CFD (Computational Fluid Dynamics) solution is often followed by a CSD (Computational Structural Dynamics) solution until convergence is achieved. Hence, this coupling approach can be less labor-intensive due to the code reusability. Large-scale FSI problems can also be conveniently solved due to the reduction of the problem size. Over the last decade, this approach has gained considerable success [17]. However, this approach may also cause some computational issues. It should be noted that the widespread implementations [17, 40] of this FSI coupling approach is to advance the fluid-structure interface by the CSD solvers, which would become unstable or divergent if large deformation is considered including both physical and geometrical nonlinearities. These nonlinearities can all be encountered in cell motion under a variety of conditions both *in vivo* and in controlled experiments on single cells [1, 41, 42]. Furthermore, CSD solvers cannot guarantee the volume conservation of the internal and ambient liquids of a cell without imposing additional constraints as done in [12]. Hence, further improvements in robustness and efficiency are needed for applying the weak coupling approach for cell motion simulation.

In this study, an alternative coupling approach is presented for large deformation fluid-structure interaction simulation of living cells. Interfacial advancement of the FSI problem is performed by the temporal integration of the interfacial velocities, which are obtained by a CFD solver. A Cauchy stresses-based CSD solver is developed to obtain the membrane load efficiently without the complexity of the conventional nonlinear CSD solvers [17, 18]. It should be noted for large deformation analysis the difference between the Cauchy stresses and the Kirchhoff stresses can be too significant [35, 43, 44] to be ignored.

The motion of a deformable cell or capsule consisting of a Newtonian fluid and enclosed by an elastic membrane in microcirculation can be represented by the interfacial velocities \mathbf{v}^{FSI} at the fluid-structure interface Γ^{FSI} . After performing a temporal integration, the structural displacements of the membrane can be obtained as

$$\mathbf{u}(t_2) = \mathbf{u}(t_1) + \int_{t_1}^{t_2} \mathbf{v}^{\text{FSI}} dt, \quad (2.8)$$

in which t_1 and t_2 indicate the start and finish times, respectively, and the time step $\Delta t = t_2 - t_1$. The temporal integration in Eq. (2.8) can be approximately implemented by several explicit or implicit time marching schemes [45]. In the present study, only the classical

fourth-order Runge-Kutta method is adopted, which can be written as follows:

$$\mathbf{u}\left(t_1 + \frac{1}{2}\Delta t\right)^* = \mathbf{u}(t_1) + \frac{1}{2}\Delta t \mathbf{v}^{\text{FSI}}(t_1), \quad (2.9a)$$

$$\mathbf{u}\left(t_1 + \frac{1}{2}\Delta t\right)^{**} = \mathbf{u}(t_1) + \frac{1}{2}\Delta t \mathbf{v}^{\text{FSI}}\left(t_1 + \frac{1}{2}\Delta t\right)^*, \quad (2.9b)$$

$$\mathbf{u}(t_2)^* = \mathbf{u}(t_1) + \Delta t \mathbf{v}^{\text{FSI}}\left(t_1 + \frac{1}{2}\Delta t\right)^{**}, \quad (2.9c)$$

$$\begin{aligned} \mathbf{u}(t_2) = \mathbf{u}(t_1) + \frac{1}{6}\Delta t \left(\mathbf{v}^{\text{FSI}}(t_1) + 2\mathbf{v}^{\text{FSI}}\left(t_1 + \frac{1}{2}\Delta t\right)^* \right. \\ \left. + 2\mathbf{v}^{\text{FSI}}\left(t_1 + \frac{1}{2}\Delta t\right)^{**} + \mathbf{v}^{\text{FSI}}(t_2) \right), \end{aligned} \quad (2.9d)$$

in which $\mathbf{v}^{\text{FSI}}(t_1 + \frac{1}{2}\Delta t)^*$ and $\mathbf{v}^{\text{FSI}}(t_1 + \frac{1}{2}\Delta t)^{**}$ are the velocities at time $t_1 + \frac{1}{2}\Delta t$ predicted by the present fluid solver with respect to the configurations $\mathbf{u}(t_1 + \frac{1}{2}\Delta t)^*$ and $\mathbf{u}(t_1 + \frac{1}{2}\Delta t)^{**}$, respectively. It can be seen that the first two steps use an explicit Euler predictor and an implicit corrector at time $t_1 + \frac{1}{2}\Delta t$. The third step applies a midpoint rule predictor for the full step and the last step uses a Simpson's rule corrector to obtain the fourth-order accuracy [45]. Hence, this method can be more accurate than the explicit Euler's method, which was adopted for simulating cell motion in [3, 4].

Hence, after solving Eq. (2.8), the unknowns in Eq. (2.7) are the membrane load \mathbf{f}^s only since the Cauchy stress tensor $\sigma(t_2)$ can be a function of the structural displacements $\mathbf{u}(t_1)$, i.e.

$$\mathbf{f}^s(t_2) = -\text{div}\sigma(t_2) = -\text{div}\sigma(\mathbf{u}(t_2)). \quad (2.10)$$

Therefore, the numerical difficulties in solving a system of nonlinear equations due to the large deformation of living cells can be avoided. The computational efficiency can be significantly improved and the numerical instability issue is greatly alleviated since the most time-consuming nonlinear equations solving step in a nonlinear structural mechanics solver [35, 43, 44] is avoided. According to Newton's third law, the traction forces in Eq. (2.6) can be given as

$$\mathbf{f}^f(t_2) = -\mathbf{f}^s(t_2). \quad (2.11)$$

Hence, the fluid velocity vector $\mathbf{v}(t_2)$ and scalar pressure $p(t_2)$ can be obtained by solving Eq. (2.6). After updating the interfacial velocity vector \mathbf{v}^{FSI} , simulation for the next time step can be similarly performed. This procedure will continue until the convergence or the maximum number of time steps is reached.

It is evident that to perform the present FSI simulation smoothly, efficient structural mechanics and fluid mechanics solvers are necessary to discretize the continuous governing equations (2.10) and (2.6), respectively. In this study, as shown in Fig. 2, an efficient implementation of the present coupling approach is developed based on an FEM solver for the cell membranes and a BEM solver for the biological fluids.

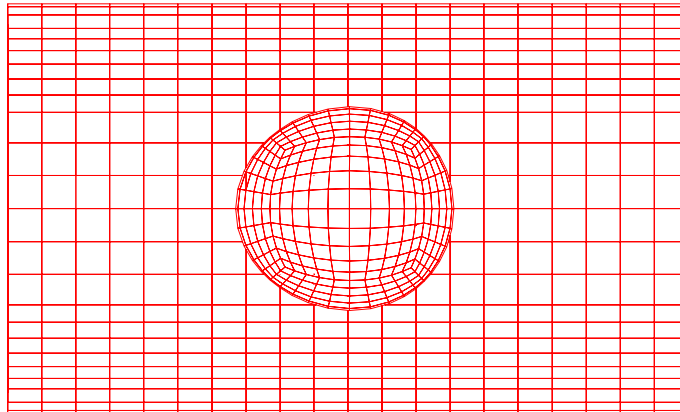


Figure 2: BEM/FEM discretization for cell motion in a circular cylinder.

2.2 FEM-based structural mechanics solver

The typical size of a suspended moving cell is $10\ \mu\text{m}$ while the thickness of its membrane is less than $10\ \text{nm}$ [46, 47]. Hence, the aspect ratio of a cell membrane is quite small. The plasma membrane envelops the cell, separates its interior from its environment and serves as a filter and communications beacon. The membrane is made mostly from a double layer of lipids and hydrophilic phosphorus molecules [48]. Embedded within this membrane is a variety of protein molecules that act as channels and pumps that move different molecules into and out of the cell. Although the micro/nanostructural/molecular dynamics approach [6, 14, 15, 49] has been used to investigate the membrane cytoskeletal mechanics, it is still a challenge to study single cell mechanics when taking the living and dynamic nature of the cell into consideration [15]. On the other hand, the continuum approach [15] can greatly simplify the numerical and experimental analysis since the whole cell is assumed to be homogeneous without the complicated cytoskeleton. In this study, the continuum approach is adopted and the cell membrane is further approximated as an isotropic thin shell [3, 4, 11, 15, 42].

The finite element method can be used for the static and dynamic response analysis of a thin shell. Several classes of thin shell elements are available in the literature [50–55], including the curved shell elements, the flat shell elements, the degenerate solid shell elements and the solid shell element. All these elements have their own advantages and disadvantages in terms of accuracy, efficiency, robustness and ease of implementation. In this study, the quadrilateral flat shell element [53] is employed and thus the continuously curved cell membrane is actually modeled as an assembly of small quadrilateral flat elements, as shown in Fig. 3, in which flat shell elements are used to discretize a spherical cell. It should be noted that the flat shell element approximation gives very adequate solutions for many practical problems [51–54] since the geometrical discretization error can be approximately of the same order as the field discretization of other low-order shell elements [52].

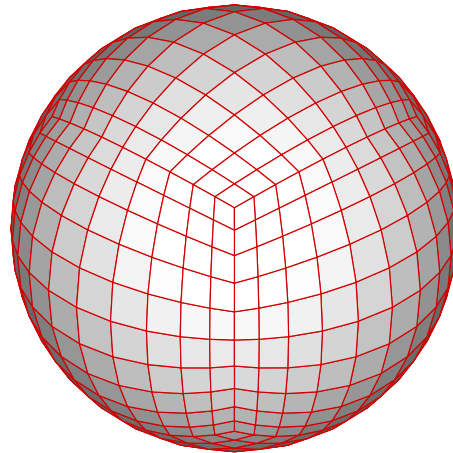


Figure 3: Flat shell elements for a spherical cell.

The structural mechanics governing equations (2.7) are nonlinear with respect to both the geometry and the material. The corresponding finite element formulation can be established in terms of a weak form [43, 52, 56] of these differential equations (2.7) under the current configuration (at time t_2), which can be given as follows:

$$\int_{\Omega^s(t_2)} \mathbf{f}^s(t_2) \cdot \delta \hat{\mathbf{u}} d\Omega = \int_{\Omega^s(t_2)} \boldsymbol{\sigma}(t_2) : \delta \hat{\boldsymbol{\epsilon}}(t_2) d\Omega, \quad (2.12)$$

where $\hat{\mathbf{u}}$ is the virtual displacement vector, $\hat{\boldsymbol{\epsilon}}$ is the virtual velocity gradient tensor, and “:” indicates double product or double contract of two tensors [56]. The virtual velocity gradient tensor is related with the virtual displacement vector as

$$\hat{\boldsymbol{\epsilon}} = \frac{1}{2} \left(\nabla \hat{\mathbf{u}} + (\nabla \hat{\mathbf{u}})^T \right). \quad (2.13)$$

The relationship between the Cauchy stress tensor and the structural deformation can be described by a solid material constitutive model. There are several material models available for the continuum cell membrane [4, 11]. One of the most often used models is Rivlin’s neo-Hookean material model, which assumes that the Cauchy stresses due to deformation are proportional to the Finger tensor \mathcal{B} as

$$\boldsymbol{\sigma} = -\hat{p} \mathbf{I} + G \mathcal{B}, \quad (2.14)$$

where \hat{p} is the pressure ($= \frac{1}{3} \text{tr}(\boldsymbol{\sigma})$), \mathbf{I} the unity tensor, and G the shear modulus. The Finger tensor \mathcal{B} is defined as the inverse of the Left Cauchy-Green deformation tensor as

$$\mathcal{B} = \left(\mathbf{F} \mathbf{F}^T \right)^{-1} \quad (2.15)$$

in which \mathbf{F} is the deformation gradient tensor [56]. For general elastic capsule membranes and/or for the membrane of a red blood cell, other continuum constitutive models [3,4,11,57–60] based on different strain energy functions have been proposed. Numerical complexity as well as ambiguity may thus be introduced. On the other hand, large deformation including large (finite) displacements but small strains can be quite common in a large class of cell motion problems in which the rigid body translational and rotational displacements are dominated [1,47]. Due to the small strains, the linear elasticity theory and the hyperelasticity theories based on different strain energy functions will give similar solutions, as shown in [1]. It should also be noted that a hyperelastic material based on the neo-Hookean model (2.14) will initially be linear. In order to focus the present study on an efficient FSI coupling approach rather than an appropriate solid material constitutive model, only the linear elasticity theory is adopted thereafter and the relationship between the Cauchy stress tensor $\boldsymbol{\sigma}$ and the linearized Eulerian or Almansi strain tensor $\boldsymbol{\varepsilon}$ can be expressed as the following linear constitutive equations:

$$\boldsymbol{\sigma} = \mathcal{C} : \boldsymbol{\varepsilon}, \quad (2.16)$$

where \mathcal{C} is the symmetric fourth-order Lagrangian elasticity tensor [56], and the linearized Eulerian or Almansi strain tensor $\boldsymbol{\varepsilon}$ can be given as

$$\boldsymbol{\varepsilon} = \frac{1}{2} \left(\nabla \mathbf{u} + (\nabla \mathbf{u})^T \right). \quad (2.17)$$

A typical quadrilateral flat shell element in a local Cartesian coordinate system subject simultaneously to membrane and bending actions is shown in Fig. 4. It can be seen that the flat shell element is constructed by combining an in-plane membrane element with a plate bending element. Membrane-bending coupling has only been neglected locally and may occur on the interelement boundary [51,52].

The present quadrilateral membrane element as shown in Figs. 4(a) and 4(b) is isoparametric. The mapping between the local spatial coordinates (\bar{x}, \bar{y}) and the natural coordinates (ζ, η) can be written as

$$\begin{Bmatrix} \bar{x} \\ \bar{y} \end{Bmatrix} = \mathbf{N}(\zeta, \eta) \bar{\mathbf{x}}^e, \quad (2.18a)$$

where

$$\mathbf{N} = [N_1 \mathbf{I}^m \quad N_2 \mathbf{I}^m \quad N_3 \mathbf{I}^m \quad N_4 \mathbf{I}^m], \quad \mathbf{I}^m \in \mathbb{R}^{2 \times 4}, \quad (2.18b)$$

$$\begin{cases} N_1 = \frac{1}{4}(1+\zeta)(1+\eta), \\ N_2 = \frac{1}{4}(1+\zeta)(1-\eta), \\ N_3 = \frac{1}{4}(1-\zeta)(1-\eta), \\ N_4 = \frac{1}{4}(1-\zeta)(1+\eta), \end{cases} \quad (2.18c)$$

$$\bar{\mathbf{x}}_i^e = \begin{Bmatrix} \bar{x}_i \\ \bar{y}_i \end{Bmatrix}, \quad i = 1, 2, 3, 4. \quad (2.18d)$$

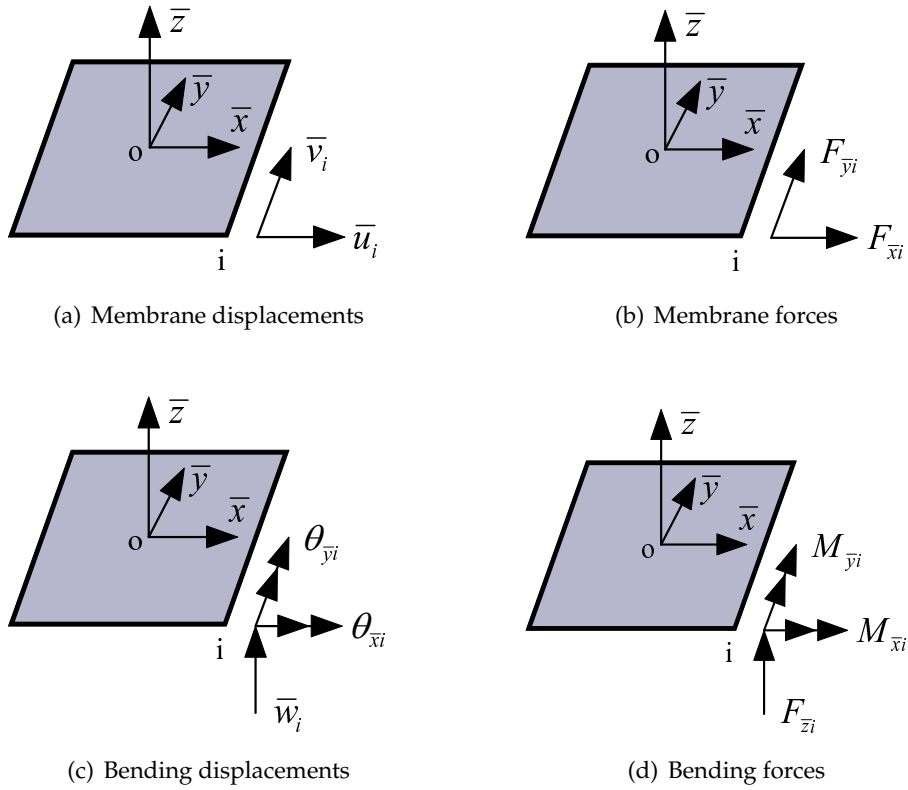


Figure 4: A flat shell element subject to membrane and bending actions.

The membrane displacements $\bar{\mathbf{u}}^m$ can be represented as

$$\bar{\mathbf{u}}^m = \mathbf{N}(\xi, \eta) (\bar{\mathbf{a}}^e)^m, \tag{2.19a}$$

where

$$(\bar{\mathbf{a}}^e)^m = \left\{ \begin{matrix} \bar{u}_i \\ \bar{v}_i \end{matrix} \right\}. \tag{2.19b}$$

According to Eqs. (2.12), (2.16) and (2.17), the nodal membrane forces $(\bar{\mathbf{f}}^e)^m$ in the local coordinate system can be finally obtained as

$$(\bar{\mathbf{f}}^e)^m = (\bar{\mathbf{K}}^e)^m (\bar{\mathbf{a}}^e)^m, \tag{2.20a}$$

where

$$(\bar{\mathbf{f}}^e)^m = \left\{ \begin{matrix} F_{\bar{x}i} \\ F_{\bar{y}i} \end{matrix} \right\}, \tag{2.20b}$$

$$(\bar{\mathbf{K}}^e)^m = h \int_{S^e(t_2)} (\mathbf{B}^m)^T \mathbf{C} \mathbf{B}^m d\bar{x}d\bar{y}, \tag{2.20c}$$

in which h is the thickness of the shell, S^e the mid-plane of the flat element, and \mathbf{B}^m the membrane strain-displacement matrix [52, 53].

Similarly, the nodal bending forces $(\bar{\mathbf{f}}^e)^b$ are related with the nodal bending displacements $(\bar{\mathbf{a}}^e)^b$ as

$$(\bar{\mathbf{f}}^e)^b = (\bar{\mathbf{K}}^e)^b (\bar{\mathbf{a}}^e)^b, \quad (\bar{\mathbf{f}}^e)_i^b = \begin{Bmatrix} F_{zi} \\ M_{\bar{x}i} \\ M_{\bar{y}i} \end{Bmatrix}, \quad (\bar{\mathbf{a}}^e)_i^b = \begin{Bmatrix} \bar{w}_i \\ \theta_{\bar{x}i} \\ \theta_{\bar{y}i} \end{Bmatrix}, \quad (2.21)$$

where $(\bar{\mathbf{K}}^e)^b$ is the bending stiffness matrix in the local coordinate system [52, 53]. Eqs. (2.20a) and (2.21) can be further assembled as

$$\bar{\mathbf{f}}^e = \bar{\mathbf{K}}^e \bar{\mathbf{a}}^e, \quad \bar{\mathbf{f}}_i^e = \begin{Bmatrix} F_{xi} \\ F_{yi} \\ F_{zi} \\ M_{\bar{x}i} \\ M_{\bar{y}i} \\ M_{\bar{z}i} \end{Bmatrix}, \quad \bar{\mathbf{a}}_i^e = \begin{Bmatrix} \bar{u}_i \\ \bar{v}_i \\ \bar{w}_i \\ \theta_{\bar{x}i} \\ \theta_{\bar{y}i} \\ \theta_{\bar{z}i} \end{Bmatrix}, \quad (2.22)$$

where $\bar{\mathbf{K}}^e$ is the element stiffness matrix in the local coordinate system, $\bar{\mathbf{f}}^e$ and $\bar{\mathbf{a}}^e$ are the local nodal forces and displacements, respectively. It should be noted that the fictitious drilling rotation $\theta_{\bar{z}i}$ and drilling moment $M_{\bar{z}i}$ are introduced as a couple for the convenience of assemblage [51, 52], which can be done by inserting an appropriate number of zeroes into the stiffness matrix.

By the rules of orthogonal transformation [52], Eq. (2.22) can be written in global coordinates as

$$\mathbf{f}^e = \mathbf{K}^e \mathbf{a}^e, \quad \mathbf{f}_i^e = \begin{Bmatrix} F_{xi} \\ F_{yi} \\ F_{zi} \\ M_{xi} \\ M_{yi} \\ M_{zi} \end{Bmatrix}, \quad \mathbf{a}_i^e = \begin{Bmatrix} u_i \\ v_i \\ w_i \\ \theta_{xi} \\ \theta_{yi} \\ \theta_{zi} \end{Bmatrix}, \quad (2.23a)$$

where

$$\mathbf{K}^e = \mathbf{T}^T(t_2) \bar{\mathbf{K}}^e \mathbf{T}(t_2) \quad (2.23b)$$

in which $\mathbf{T}(t_2)$ is the transformation matrix of the current configuration at time t_2 . The total nodal forces \mathbf{f} in the global Cartesian coordinate system can be obtained as

$$\mathbf{f} = \cup_{i=1}^N \mathbf{f}^i, \quad (2.24)$$

where N is the total number of elements.

Several numerical issues need to be addressed in order to make the present shell element robust enough for large deformation FSI simulation of cell motion. It should

be noted that the present method is based on the current configuration and thus the nodal coordinates should be updated before calculating the stiffness matrix. It is different from the conventional nonlinear finite element method, in which the displacements are unknown and the stiffness matrix is based on the previous configuration [44,52]. For thin shell elements, numerical instabilities such as shear locking and membrane locking can be significant [51, 61]. In the present study, the selective reduced integration technique [51, 62, 63] is adopted to alleviate these problems. It should also be noted that the rigid body displacements may dominate the large deformation cell motion, as aforementioned. In the finite element analysis, the existence of rigid body displacement components may severely affect the convergence rate [62, 64, 65]. In the nonlinear finite element analysis, an element may still fail to pass the rigid body test even if the patch test and eigenvalue test for the linear finite element analysis can be passed due to the initial stresses [35]. To develop a robust algorithm for the membrane load recovery, the rigid body displacements should be eliminated. Hence, different from many other implementations in the literature [1, 4, 18], only the deformational displacements are accounted for in the present force recovery as shown in Eqs. (2.23a) and (2.24).

The nodal displacement vector \mathbf{a}_i^e in Eq. (2.23a) can be decomposed as

$$\mathbf{a}_i^e = (\mathbf{a}_i^e)^R + (\mathbf{a}_i^e)^d, \quad (2.25)$$

where $(\mathbf{a}_i^e)^R$ is the rigid body displacement vector, and $(\mathbf{a}_i^e)^d$ the deformational displacement vector, which can be expressed as

$$(\mathbf{a}_i^e)^d = \left\{ \begin{array}{l} (\mathbf{a}_i^e)^t \\ (\mathbf{a}_i^e)^r \end{array} \right\}, \quad (2.26)$$

in which $(\mathbf{a}_i^e)^t$ is the deformational translations, and $(\mathbf{a}_i^e)^r$ the deformational rotations. Due to the flat shell element, according to [66], the deformational translations $(\mathbf{a}_i^e)^t$ can be given as follows:

$$(\mathbf{a}_i^e)^t = \mathbf{T}(t_2)(\mathbf{x}_i^e(t_1) + \mathbf{u}_i^e(t_2)) - \mathbf{T}(t_1)\mathbf{x}_i^e(t_1). \quad (2.27)$$

Moreover, the deformational rotations $(\mathbf{a}_i^e)^r$ can be obtained from the deformational rotation tensor $\widetilde{\mathcal{R}}$, which is related with the total rotation tensor \mathcal{R} [66] as

$$\widetilde{\mathcal{R}} = \mathbf{T}(t_2)\mathcal{R}\mathbf{T}^T(t_1), \quad (2.28a)$$

where

$$\mathcal{R} = \mathbf{I} + \frac{\sin(\varphi)}{\varphi}\mathbf{\Phi} + \frac{1}{2}\left(\frac{\sin(\varphi/2)}{\varphi/2}\right)^2\mathbf{\Phi}^2, \quad (2.28b)$$

in which $\mathbf{\Phi}$ is the spin tensor, and φ the length of the corresponding pseudo-vector of the total rotations of the i -th node [66, 67]. The theoretical formulation to extract the deformational rotation vector $(\mathbf{a}_i^e)^r$ from the tensor $\widetilde{\mathcal{R}}$ [66] is:

$$(\mathbf{a}_i^e)^r = \text{axial} \left[\ln \left(\widetilde{\mathcal{R}} \right) \right], \quad (2.29)$$

where “axial” indicates the axial vector. However, this method tends to be numerically unstable for rotation angles near 0 or $\pm\pi$, etc. [66]. A more robust procedure proposed by Spurrer [68] in the language of quaternions is thus adopted in this study, in which the algebraically largest of trace ($\widetilde{\mathcal{R}}$) and $\widetilde{\mathcal{R}}_{ii}$ was used.

Hence, the membrane force recovery in Eq. (2.23a) can be re-written in a robust manner as

$$\mathbf{f}^e = \mathbf{K}^e (\mathbf{a}^e)^d, \quad (2.30)$$

in which the rigid body displacements are excluded and thus their adverse effects on numerical convergence of the finite element method [62] can be prevented. It should be noted that the present procedure to obtain the deformational displacements is different from the co-rotational method in the nonlinear finite element analysis [66], in which only the previous configuration based on the Kirchhoff stresses is used.

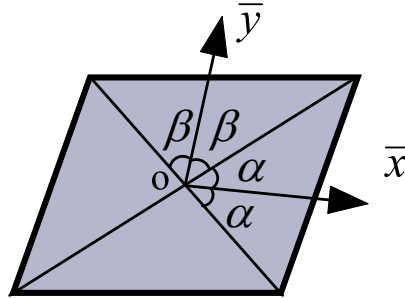


Figure 5: Determination of the local coordinate system.

According to Eqs. (2.23a) and (2.23b), the element stiffness matrix \mathbf{K}^e in the global coordinate system must be orientation invariant since the nodal force vector \mathbf{f}^e in the global coordinate system is independent of the local coordinate system. Therefore, the selection of the local coordinate system to determine the transformation matrix \mathbf{T} can be of crucial importance. Nevertheless, this issue was not fully addressed in the literature [52] since only the relatively simple triangular and rectangular elements were often dealt. It should be noted that the rectangular elements may become quadrilateral due to large deformation and thus the local coordinate system for the rectangular elements in [52] may violate the orientation invariant requirement if large deformation is taken into consideration. In this study, the local coordinate system shown in Fig. 5 is adopted. The single intersection point of the two diagonal lines of the quadrilateral is used as the local origin point and the local axes \bar{x} and \bar{y} bisect the intersecting angles of the two diagonal lines. The local axis \bar{x} and \bar{y} are perpendicular to each other since it is apparent that $\alpha + \beta = 90^\circ$, where α and β are half of the intersecting angles. The orientation invariant property of the local stiffness matrix can be guaranteed [51] since the local axes are actually independent of the numbering order of the four nodes.

The present flat shell element requires that the four nodes of a quadrilateral element be always co-planar during the large deformation FSI simulation of cell motion. Fur-

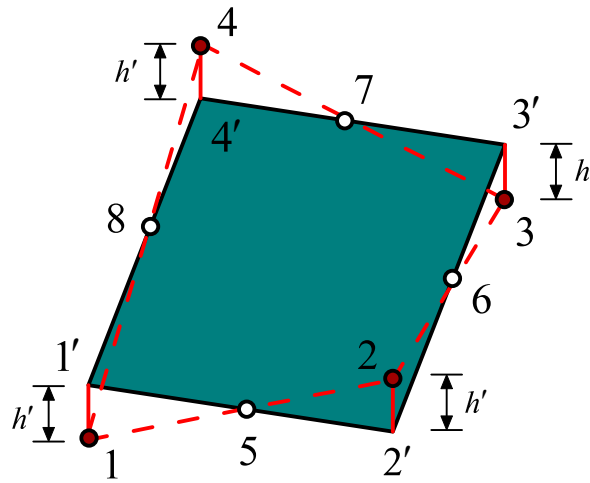


Figure 6: Geometric approximation for the non-planar element.

thermore, as later discussed, the present BEM-based fluid solver also requires that the four nodes of each panel (element) be co-planar to facilitate the boundary integration. However, this requirement cannot be exactly satisfied during the large deformation simulation, as noted by many researchers [51, 54]. To make the present algorithm for large deformation FSI simulation robust and efficient, this issue must be well tackled. In this study, further geometric approximation is introduced when the four nodes of an element are found to be non-planar. As shown in Fig. 6, although the four nodes (1, 2, 3 and 4) are non-planar, the mid-points of the four edges (5, 6, 7 and 8) can be proven to be within the same plane to which the distances of the four non-planar nodes are of the same h' . Hence, it is natural to project the non-planar nodes to the plane as the co-planar nodes $1'$, $2'$, $3'$ and $4'$. This geometric approximation of the curved shell is similar to that made by the flat shell element [51, 52] and thus the present handling can be reasonable if the mesh discretization is fine enough. As discussed in [52], in most arbitrarily shaped curved shell elements, complete smoothness of the surface between elements is not guaranteed. The shape discontinuity occurring in curved shell elements can be of the same type as that encountered in the present flat shell elements and therefore the present geometric approximation can be generally applicable.

2.3 BEM-based fluid mechanics solver

In simulating the biological fluids, the full Navier-Stokes equations may be considerably simplified as Stokes equations, as aforementioned. In the Stokes flow approximation as given in Eq. (2.6), due to the linearity of the Stokes equations, a Green's function for the equations can be found, the velocity field can be obtained by a boundary integral representation [69] derived from Green's formulae corresponding to the present Stokes

problem as

$$\mathbf{v}(\mathbf{x}') = \int_S \mathbf{G}(\mathbf{x}, \mathbf{x}') \mathbf{t}(\mathbf{x}) dS - \int_S \mathbf{T}(\mathbf{x}, \mathbf{x}') \mathbf{v}(\mathbf{x}) dS, \quad \mathbf{x}' \in \Omega^f \setminus \Omega^{\text{FSI}}, \quad (2.31)$$

where $\mathbf{t}(\mathbf{x}) = \boldsymbol{\sigma}_N(\mathbf{x}) \cdot \mathbf{n}(\mathbf{x})$ is the traction force vector, $\boldsymbol{\sigma}_N(\mathbf{x})$ the fluid Newtonian stress tensor, $\mathbf{n}(\mathbf{x})$ the outward normal vector at a point \mathbf{x} of the closed surface S , $\mathbf{G}(\mathbf{x}, \mathbf{x}')$ and $\mathbf{T}(\mathbf{x}, \mathbf{x}')$ are the velocity field and traction field of the fundamental solution of the Stokes equations respectively, which are also known as the Stokeslet and stresslet respectively [69] and can be given as

$$G_{ij}(\mathbf{x}, \mathbf{x}') = \frac{1}{8\pi\mu r} (\delta_{ij} + r_{,i} r_{,j}), \quad (2.32a)$$

$$T_{ij}(\mathbf{x}, \mathbf{x}') = \frac{3r_{,i} r_{,j}}{4\pi r^2} \frac{\partial r}{\partial n'}, \quad (2.32b)$$

in which $r = |\mathbf{x}' - \mathbf{x}|$, $r_{,j} = (x'_j - x_j)/r$, and δ_{ij} is Kronecker's delta notation.

Similarly, the scalar pressure field $p(\mathbf{x}')$ can be given as

$$p(\mathbf{x}') = \int_S \mathbf{q}(\mathbf{x}, \mathbf{x}') \cdot \mathbf{t}(\mathbf{x}) dS - \mu \int_S \mathbf{w}(\mathbf{x}, \mathbf{x}') \cdot \mathbf{v}(\mathbf{x}) dS, \quad \mathbf{x}' \in \Omega^f \setminus \Omega^{\text{FSI}}, \quad (2.33a)$$

where

$$q_j(\mathbf{x}, \mathbf{x}') = \frac{r_{,j}}{4\pi r^2}, \quad (2.33b)$$

$$w_j(\mathbf{x}, \mathbf{x}') = \frac{1}{\pi r^2} \left(n_j - r_{,j} \frac{\partial r}{\partial n} \right). \quad (2.33c)$$

Furthermore, the boundary integral equations for a point $\mathbf{x}' \in S$ can be expressed as follows:

$$\mathbf{c}(\mathbf{x}') \mathbf{v}(\mathbf{x}') = \int_S \mathbf{G}(\mathbf{x}, \mathbf{x}') \mathbf{t}(\mathbf{x}) dS - \int_S \mathbf{T}(\mathbf{x}, \mathbf{x}') \mathbf{v}(\mathbf{x}) dS, \quad (2.34a)$$

$$\Theta(\mathbf{x}') p(\mathbf{x}') = \int_S \mathbf{q}(\mathbf{x}, \mathbf{x}') \cdot \mathbf{t}(\mathbf{x}) dS - \mu \int_S \mathbf{w}(\mathbf{x}, \mathbf{x}') \cdot \mathbf{v}(\mathbf{x}) dS, \quad (2.34b)$$

where $\mathbf{c}_{ij}(\mathbf{x}') = \Theta(\mathbf{x}') \delta_{ij}$ and $\Theta(\mathbf{x}')$ is the internal angle at point \mathbf{x}' [69]. It should be noted that the first integral in Eq. (2.34a) is weakly singular since its singularity is of order $\mathcal{O}(r^{-1})$ while the second integral is strongly singular due to its singularity order $\mathcal{O}(r^{-2})$. Furthermore, the first integral in Eq. (2.34b) is strongly singular ($\mathcal{O}(r^{-2})$) while the second integral is hypersingular ($\mathcal{O}(r^{-3})$). Hence, special care must be taken to perform the singularity integration, which is usually complicated to implement.

The boundary integral equations (2.34a) and (2.34b) can be solved by the boundary element method (BEM), or panel method [70]. In this study, a low-order panel method is developed, in which the closed boundary surface S is represented by an ensemble of flat quadrilateral panels, the unknowns are assumed to be constant over each panel, and the boundary integral equations are enforced at the centroid of each panel as a collocation method [70]. As shown in Fig. 2, there is a one-to-one coincidence between the BEM panel and the FEM element at the cell surface to achieve the consistency and compatibility for the BEM/FEM coupling. Applying the specified surface velocities and traction forces as the boundary conditions, the unknown surface velocities and traction forces can be obtained by using standard BEM formulations [69] based on Eq. (2.34a) only, in which the singularity integration over each low-order panel can be analytically performed [70]. The pressure field can then be calculated by using Eq. (2.33a). However, the higher-order singularity of the pressure kernels in Eq. (2.33a) may pose the numerical integration difficulty. In this study, a regularization method [69] for reducing the dominant singularity is adopted. It should be noted that the velocities at the membrane surface of the cell can satisfy the mass continuity condition and thus the cell volume can be well kept constant after the time advancement of the membrane surface using the classical Runge-Kutta method in Eq. (2.9) with a relatively small time step, as reported in [4].

For the exterior fluid (plasma) of a cell, applying the present BEM discretization to the boundary integral equation (2.34a) yields

$$\mathbf{c}_i(\mathbf{x}'_i) \mathbf{v}(\mathbf{x}'_i) = \sum_{j=1}^{NE} \mathbf{t}(\mathbf{x}_j) \int_{S_j} \mathbf{G}(\mathbf{x}, \mathbf{x}'_i) dS - \sum_{j=1}^{NE} \mathbf{v}(\mathbf{x}_j) \int_{S_j} \mathbf{T}(\mathbf{x}, \mathbf{x}'_i) dS, \quad (2.35)$$

where \mathbf{x}'_i is the centroid of the i -th panel, and NE the total number of panels. Due to the point collocation method, linear algebraic equations can be derived from Eq. (2.35) as

$$(\mathbf{C} + \mathcal{T}) \mathbf{v} - \mathcal{G} \mathbf{t} = \mathbf{0}, \quad (2.36a)$$

where

$$\mathbf{C} = \text{diag}\{\mathbf{c}_1(\mathbf{x}'_1), \mathbf{c}_2(\mathbf{x}'_2), \dots, \mathbf{c}_N(\mathbf{x}'_N)\}, \quad (2.36b)$$

$$\mathbf{v} = \{\mathbf{v}(\mathbf{x}'_1), \mathbf{v}(\mathbf{x}'_2), \dots, \mathbf{v}(\mathbf{x}'_N)\}, \quad (2.36c)$$

$$\mathbf{t} = \{\mathbf{t}(\mathbf{x}'_1), \mathbf{t}(\mathbf{x}'_2), \dots, \mathbf{t}(\mathbf{x}'_N)\}, \quad (2.36d)$$

$$\mathcal{T}_{ij} = \int_{S_j} \mathbf{T}(\mathbf{x}, \mathbf{x}'_i) dS, \quad (2.36e)$$

$$\mathcal{G}_{ij} = \int_{S_j} \mathbf{G}(\mathbf{x}, \mathbf{x}'_i) dS. \quad (2.36f)$$

In Eq. (2.36a), the total number of equations is N while the total number of unknowns is $2N$. Hence, the boundary conditions of the surface must be taken into account. The

surface S can be expressed as

$$S = S_v \cup S_t \cup S_c \quad (2.37)$$

in which

$$S_v \cap S_t = \emptyset, \quad S_v \cap S_c = \emptyset, \quad S_t \cap S_c = \emptyset, \quad (2.38)$$

S_v is the velocity prescribed surface such as the non-slip and non-penetration wall, S_t the traction prescribed surface such as the traction-free outlet surface, S_c the cell surface. Hence, the surface velocities and traction forces can be composed of their corresponding components on at these surfaces as

$$\mathbf{v} = \{\mathbf{v}_v, \mathbf{v}_t, \mathbf{v}_c\}, \quad (2.39a)$$

$$\mathbf{t} = \{\mathbf{t}_v, \mathbf{t}_t, \mathbf{t}_c\}, \quad (2.39b)$$

in which \mathbf{v}_v and \mathbf{t}_t are prescribed due to the boundary conditions.

Substituting Eqs. (2.39a) and (2.39b) into Eq. (2.36a) generates the following equations:

$$(\mathbf{C}_{vt} + \mathcal{T}_{vt})\mathbf{v}_t + (\mathbf{C}_{vc} + \mathcal{T}_{vc})\mathbf{v}_c - \mathcal{G}_{vv}\mathbf{t}_v - \mathcal{G}_{vc}\mathbf{t}_c = -(\mathbf{C}_{vt} + \mathcal{T}_{vt})\mathbf{v}_v + \mathcal{G}_{vt}\mathbf{t}_t, \quad (2.40a)$$

$$(\mathbf{C}_{tt} + \mathcal{T}_{tt})\mathbf{v}_t + (\mathbf{C}_{tc} + \mathcal{T}_{tc})\mathbf{v}_c - \mathcal{G}_{tv}\mathbf{t}_v - \mathcal{G}_{tc}\mathbf{t}_c = -(\mathbf{C}_{tv} + \mathcal{T}_{tv})\mathbf{v}_v + \mathcal{G}_{tt}\mathbf{t}_t, \quad (2.40b)$$

$$(\mathbf{C}_{ct} + \mathcal{T}_{ct})\mathbf{v}_t + (\mathbf{C}_{cc} + \mathcal{T}_{cc})\mathbf{v}_c - \mathcal{G}_{cv}\mathbf{t}_v - \mathcal{G}_{cc}\mathbf{t}_c = -(\mathbf{C}_{cv} + \mathcal{T}_{cv})\mathbf{v}_v + \mathcal{G}_{ct}\mathbf{t}_t, \quad (2.40c)$$

where

$$\mathbf{C} = \begin{bmatrix} \mathbf{C}_{vv} & \mathbf{C}_{vt} & \mathbf{C}_{vc} \\ \mathbf{C}_{tv} & \mathbf{C}_{tt} & \mathbf{C}_{tc} \\ \mathbf{C}_{cv} & \mathbf{C}_{ct} & \mathbf{C}_{cc} \end{bmatrix}, \quad (2.40d)$$

$$\mathcal{T} = \begin{bmatrix} \mathcal{T}_{vv} & \mathcal{T}_{vt} & \mathcal{T}_{vc} \\ \mathcal{T}_{tv} & \mathcal{T}_{tt} & \mathcal{T}_{tc} \\ \mathcal{T}_{cv} & \mathcal{T}_{ct} & \mathcal{T}_{cc} \end{bmatrix}, \quad (2.40e)$$

$$\mathcal{G} = \begin{bmatrix} \mathcal{G}_{vv} & \mathcal{G}_{vt} & \mathcal{G}_{vc} \\ \mathcal{G}_{tv} & \mathcal{G}_{tt} & \mathcal{G}_{tc} \\ \mathcal{G}_{cv} & \mathcal{G}_{ct} & \mathcal{G}_{cc} \end{bmatrix}. \quad (2.40f)$$

It can be seen that Eq. (2.40) cannot be solved independently since the total number of equations and that of unknowns are not equal. Hence, the coupling effect of the interior fluid (cytoplasm) of the cell must be considered.

For the interior fluid of the cell, linear algebraic equations similar to Eq. (2.36a) can be derived as follows:

$$(\tilde{\mathbf{C}} + \tilde{\mathcal{T}})\tilde{\mathbf{v}}_c - \tilde{\mathcal{G}}\tilde{\mathbf{t}}_c = \mathbf{0}, \quad (2.41)$$

where $\tilde{\mathbf{v}}_c$ and $\tilde{\mathbf{t}}_c$ are the velocities and traction forces of the interior fluid at the cell membrane surface due to the fact that the membrane encloses the whole interior fluid.

Assuming non-slip and non-penetration boundary conditions for the membrane surface, and applying Newton's third law as shown in Eq. (2.11), the continuity condition at the membrane surface can be written as

$$\tilde{\mathbf{v}}_c = \mathbf{v}_c, \quad \tilde{\mathbf{t}}_c + \mathbf{t}_c = -\mathbf{f}^*, \quad (2.42)$$

where \mathbf{f}^* is the total membrane load intensity vector in the global Cartesian coordinate system at the centroid of each panel, which is an averaged effect on each panel of the corresponding nodal forces \mathbf{f} as shown in Eq. (2.24) due to the present flat shell element solver. Hence, Eq. (2.41) can be re-written as

$$\left(\tilde{\mathbf{C}} + \tilde{\mathcal{T}} \right) \mathbf{v}_c + \tilde{\mathcal{G}} \mathbf{t}_c = -\tilde{\mathcal{G}} \mathbf{f}^*. \quad (2.43)$$

It can be seen that Eqs. (2.40) and (2.43) may be solved simultaneously since the number of equations and the number of unknowns are equal. For the purpose of simplicity, Eqs. (2.40) and (2.43) can be written in compact form as

$$\mathcal{H} \mathbf{z} = \mathbf{q}, \quad (2.44a)$$

where

$$\mathcal{H} = \begin{bmatrix} \mathbf{C}_{vt} + \mathcal{T}_{vt} & \mathbf{C}_{vc} + \mathcal{T}_{vc} & -\mathcal{G}_{vv} & -\mathcal{G}_{vc} \\ \mathbf{C}_{tt} + \mathcal{T}_{tt} & \mathbf{C}_{tc} + \mathcal{T}_{tc} & -\mathcal{G}_{tv} & -\mathcal{G}_{tc} \\ \mathbf{C}_{ct} + \mathcal{T}_{ct} & \mathbf{C}_{cc} + \mathcal{T}_{cc} & -\mathcal{G}_{cv} & -\mathcal{G}_{cc} \\ \mathbf{0} & \tilde{\mathbf{C}} + \tilde{\mathcal{T}} & \mathbf{0} & \tilde{\mathcal{G}} \end{bmatrix}, \quad (2.44b)$$

$$\mathbf{z} = \{ \mathbf{v}_t, \mathbf{v}_c, \mathbf{t}_v, \mathbf{t}_c \}, \quad (2.44c)$$

$$\mathbf{q} = \begin{Bmatrix} -(\mathbf{C}_{vt} + \mathcal{T}_{vt}) \mathbf{v}_v + \mathcal{G}_{vt} \mathbf{t}_t \\ -(\mathbf{C}_{tv} + \mathcal{T}_{tv}) \mathbf{v}_v + \mathcal{G}_{tt} \mathbf{t}_t \\ -(\mathbf{C}_{cv} + \mathcal{T}_{cv}) \mathbf{v}_v + \mathcal{G}_{ct} \mathbf{t}_t \\ -\tilde{\mathcal{G}} \mathbf{f}^* \end{Bmatrix}. \quad (2.44d)$$

The resulting linear system of equations (2.44a) is of the standard form of the boundary element method [69] with a fully populated pseudo-stiffness matrix \mathcal{H} . The conventional direct methods based on Gauss elimination to solve this system of equations are robust, but may require $\mathcal{O}(N^3)$ computations, where N is the total number of unknowns in Eq. (2.44a). For large problems the iterative methods are generally preferred to reduce the computational time [70]. In this study, the iterative GMRES (generalized minimal residual) method developed by Saad and Martin [71] is employed as a good compromise between efficiency and robustness. The GMRES method approximates the solution by the vector in a Krylov subspace with minimal residual and the Arnoldi iteration is used to find this vector. It should be noted that the computational cost and memory allocation space may be further reduced by employing some acceleration algorithms such as the pFFT (precorrected Fast Fourier Transform) method by Phillips and White [72] and the FMM (Fast Multipole method) by Greengard and Rokhlin [73]. Further incorporation of these acceleration algorithms into the present FSI simulation is under investigation.

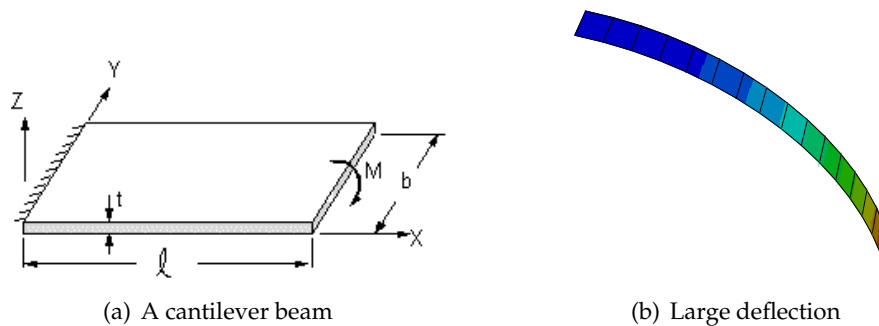


Figure 7: Large deflection of a cantilever beam.

3 Examples and discussion

Numerical examples are provided to illustrate the efficiency and accuracy and robustness of the present method. Unless stated otherwise, all the units are consistent. For all examples, the computation is terminated when the relative difference of maximum velocity between two successive iterations is less than 10^{-5} or when the prescribed maximum number of iterations has been reached. The classical cantilever beam with large rotation [74] due to pure bending is used to verify the accuracy of the present shell element for external load recovery, and to show the effect of rigid body displacements. The example of cell motion in a circular cylinder in [4] is adopted to demonstrate the accuracy, efficiency and robustness of the present BEM/FEM coupling approach for FSI simulation of cell motion.

3.1 External load recovery of a cantilever beam with large deflection

The classical cantilever [74] shown in Fig. 7 is used to verify the accuracy of the present shell element for external load recovery. The cantilever beam is of length $\ell = 12$ mm, width $b = 1$ mm, thickness $t = 1$ mm, fixed at one end and subjected to a pure bending moment $M = 15.708$ N-mm at the free end. The material properties are: Young's modulus $E = 1800$ N/m², and Poisson's ratio $\nu = 0$. The large displacements predicted in [74] due to the large rotation are used to obtain the applied load.

The bending moment M obtained by the present method is shown in Table 1. It can be seen that excellent convergence is achieved when the deformational displacements are used to calculate the external load of the cantilever beam based on Eq. (2.30). Since this is a typical problem with large displacements but small strains [55, 74], rigid body displacements can be dominated and thus the convergence speed is quite slow when using the total displacements. This is generally expected by the finite element theory [62, 63, 65, 75]. Hence, the present solutions agree well with the theoretical prediction and the accuracy of the present method can be verified.

Table 1: Bending moment M (N-mm) predicted by the present finite element method.

Mesh	M (deformational displacements)	M (total displacements)
2×1	15.652	157.968
16×1	15.706	47.100

3.2 Cell motion in a cylindrical fluid flow

The numerical example of cell motion in [4], as shown in Fig. 1, is adopted to illustrate the improvements of the present FSI simulation method in accuracy, efficiency and robustness over the existing methods. In the numerical simulations presented in [4], the cylinder was truncated at the length $L = \pi R$ to achieve a good compromise between the truncation error and the discretization error of the cylinder surface [33]. The cell motion is followed by a frame of reference moving with the mean cell velocity. The representative value are: $Et = 4.2 \times 10^{-3}$ dyn/cm, and the fluid viscosity $\mu = 1.2$ mPa-s for the interior and exterior fluids. At the initial instant, the cell is assigned a specified unstressed shape. As soon as the simulation begins, the cell is impulsively subjected to a pressure drop between the inlet and outlet. In this study, the initial cell shape is assumed to be either spherical or biconcave to facilitate a comparison study. The surfaces of the cylinder wall, inlet, outlet and the cell membrane are discretized by the BEM panels, as shown in Fig. 2, in which the BEM panels are coincident with the FEM mesh at the membrane surface.

Moving cells with initially spherical unstressed shapes of radius r at the centreline of the cylinder along the x direction are first considered. Since bending moments of the cell membranes were neglected in [4], the present method ignoring the bending moments as shown in Fig. 4 and Eq. (2.21) is used to perform a numerical comparison and to study the importance of bending stiffness of a cell membrane.

Fig. 8 shows the shape variation for a spherical cell whose radius r is equal to half the cylinder's radius R , i.e. the radius ratio is $\delta = r/R = 0.5$, and for the reduced mean velocity $G = 0.00667$ [4], in which

$$G = \frac{\mu U_M \delta}{E}, \quad (3.1)$$

where U_M is the mean velocity of the unidirectional Poiseuille flow [4], which can be given as

$$U_M = \frac{\Delta p R^2}{L 8\mu}. \quad (3.2)$$

Hence, the pressure drop Δp for this case can be obtained as

$$\Delta p = \frac{8\mu L U_M}{R^2}, \quad (3.3)$$

which is $\Delta p = 0.0337$ dyn/cm² based on the prescribed data [4]. Comparing the present 3D evolving shapes with the 2D evolving profiles in [4], it can be seen that good agreement has been reached. Furthermore, Fig. 9 shows the convergence history of the magnitude of the relative velocity (relative to the mean cell velocity) of the frontmost point

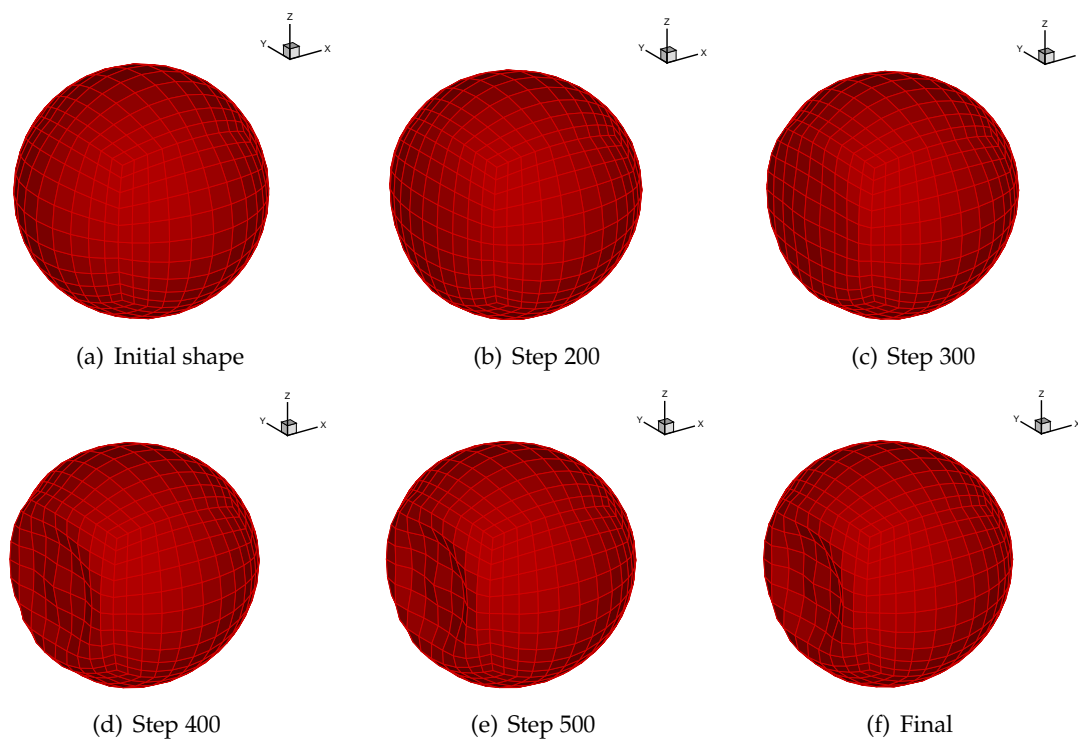


Figure 8: Shape variation of a spherical cell in a circular cylinder using a membrane forces model.

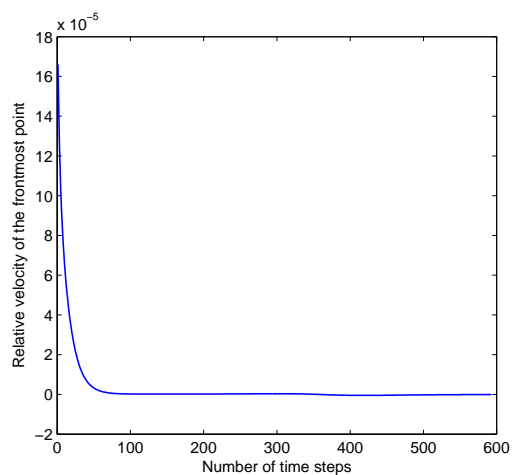


Figure 9: Convergence history of the relative velocity using a membrane forces model.

at the cell membrane. It can be seen that fast convergence can be achieved and extra iterations (about 500 timesteps) have not destroyed the numerical stability of the present FSI simulation. As a comparison, the simulation in [4] converged very slowly (more than

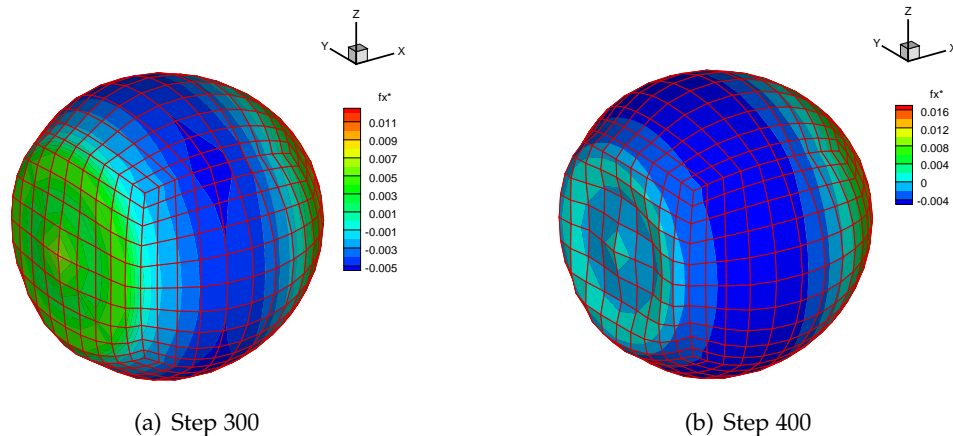


Figure 10: Membrane load component f_x^* for the membrane forces model.

1000 steps) and irregular shapes would be generated if more iterations were carried out since Euler's forward time marching scheme adopted in [4] tends to be unstable if the timestep size is not small enough. The distinct efficiency and robustness of the present method for cell motion simulation due to present improvements as aforementioned can thus be illustrated.

Simulation results shown in Fig. 8 may pose some arguments over the appropriateness of using a membrane forces model [4] for the present cell motion simulation. The shape variation at the rear of the spherical cell may suggest that a local buckling of the membrane has been generated during the cell motion [4]. As shown in Fig. 10(a), the local pressure load at the rear of the membrane is relatively high and the local surface is developed to be almost flat. Since bending stiffness is ignored in the membrane forces model, the nearly flat rear surface of the membrane can hardly withstand the transverse pressure load, and local buckling of the membrane may thus occur as shown in Fig. 10(b), totally different from the curved shell in which the membrane forces themselves can resist the pressure due to the curvature of the shell [51, 55, 62, 76]. It should be noted that in the postbuckling configuration with a concave in Fig. 10(b), the local pressure load on the concave surface has been drastically reduced.

Due to the significant local buckling on the nearly flat surfaces of a shell, the membrane forces model [4] would be inappropriate for simulating the present cell motion problem. Hence, the present method incorporating both the membrane and the bending forces as shown in Fig. 4 is applied for the cell motion simulation. The final shape is shown in Fig. 11 and the convergence history of the relative velocity of the frontmost point is shown in Fig. 12. It can be seen that the membrane deformation can be negligible due to the existence of bending stiffness in the present method. The efficiency and robustness of the present method is again demonstrated in Fig. 12. The enhanced capacity of local buckling resistance of the present flat shell element is further demonstrated

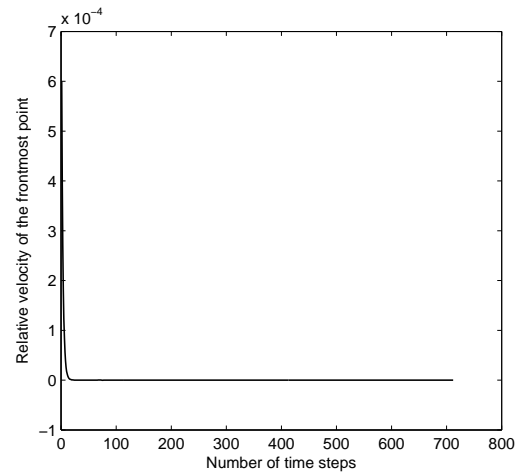
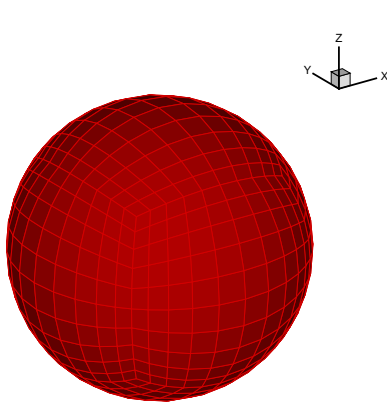


Figure 11: Final shape of the spherical cell using the present bending forces model.

Figure 12: Convergence history of the relative velocity using the present bending forces model.

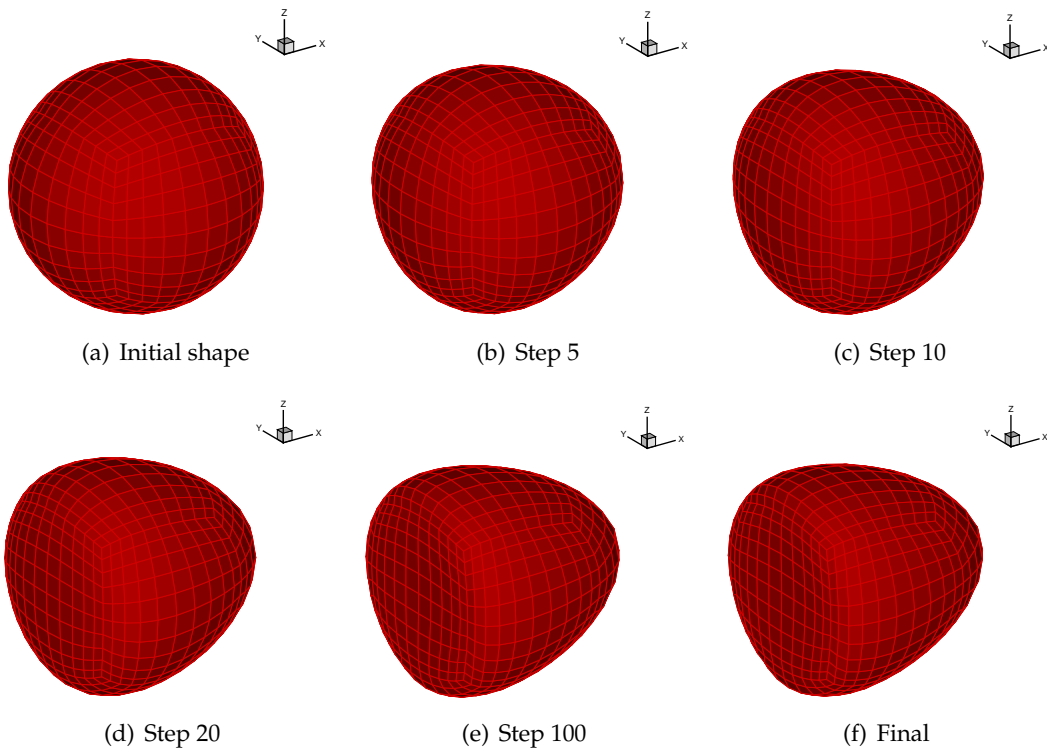


Figure 13: Shape variation of a spherical cell in a circular cylinder due to a large pressure drop.

in Fig. 13, in which the pressure drop was assumed to be 30 times larger ($\Delta p = 1.011 \text{ dyn/cm}^2$). It can be seen the membrane deformation becomes much larger due to the large pressure drop. There is no local buckling arising from a nearly flat surface evolved

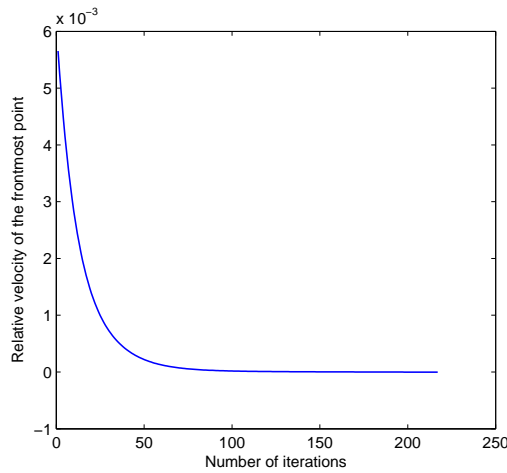


Figure 14: Convergence history of the relative velocity due to a large pressure drop.

at the rear of the cell membrane for this case due to the existence of bending stiffness in each flat shell element of the present method. Fig. 14 displays the convergence history of the relative velocity of the frontmost point of the cell membrane. It can be seen that the velocity converges quite fast. The robustness and efficiency of the present method are thus further demonstrated.

The effect of the initial position of the cell on cell motion is shown in Fig. 15, in which the cell was initially located at the xz plane with a deviation of one quarter of the cylinder radius R from the centreline axis x , yielding a nonaxisymmetric flow that is symmetric with respect to the xy plane. It can be seen that the deviated cell moves towards the centreline and the final shape can be similar to the one without initial position deviation as shown in Fig. 13. Hence, the relatively small deviation of the initial position will not affect the final axisymmetric shape of the cell and the final cylindrical flow can still be axisymmetric, as theoretically predicted [4]. The corresponding convergence history is shown in Fig. 16 and it can be seen that rapid convergence has also been achieved for this case due to the present FSI simulation method.

Moving cells with initially biconcave unstressed shapes at the centreline of the cylinder along the x direction are next considered. The biconcave resting shape is a typical shape of red blood cells [57, 59]. The membrane forces model in [4] is first adopted to facilitate a numerical comparison. The pressure drop is also assumed to be $\Delta p = 0.0337$ dyn/cm². Figure displays the shape variation of the initially biconcave cell whose initial surface can be described as

$$x = R_0 \sqrt{1 - (y^2 + z^2) / R_0^2} \left(c_0 + c_1 (y^2 + z^2) / R_0^2 + c_2 (y^2 + z^2)^2 / R_0^4 \right), \quad (3.4)$$

where $R_0 = 3.91 \mu\text{m}$, $c_0 = 0.1035805$, $c_1 = 1.001279$, and $c_2 = -0.561381$ [14]. The final shape with a convex at the front and a concave at the rear is quite similar to the one in [4] due to the similar membrane forces model. Fig. 18 shows the final results using the present

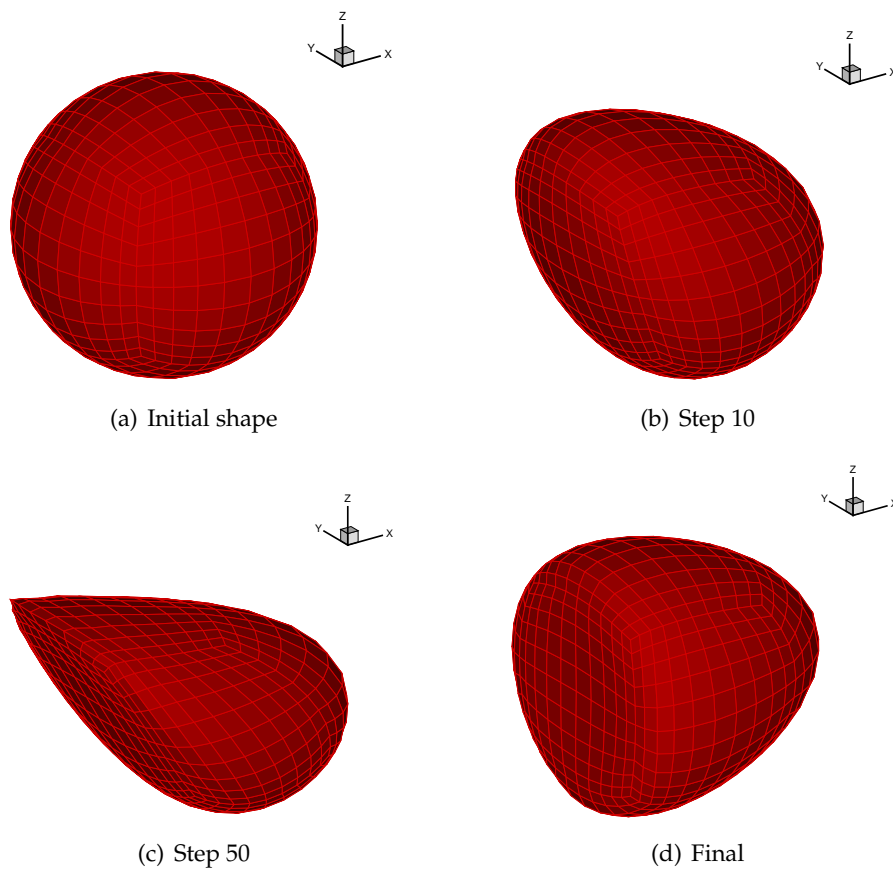


Figure 15: Shape variation of a spherical cell in a circular cylinder due to an initial position deviation.

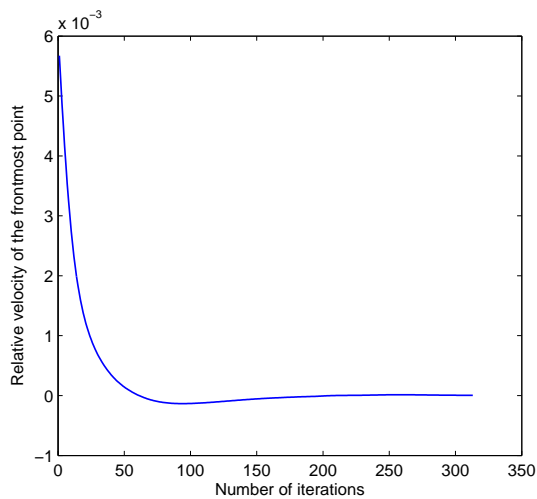


Figure 16: Convergence history of the relative velocity due to an initial position deviation.

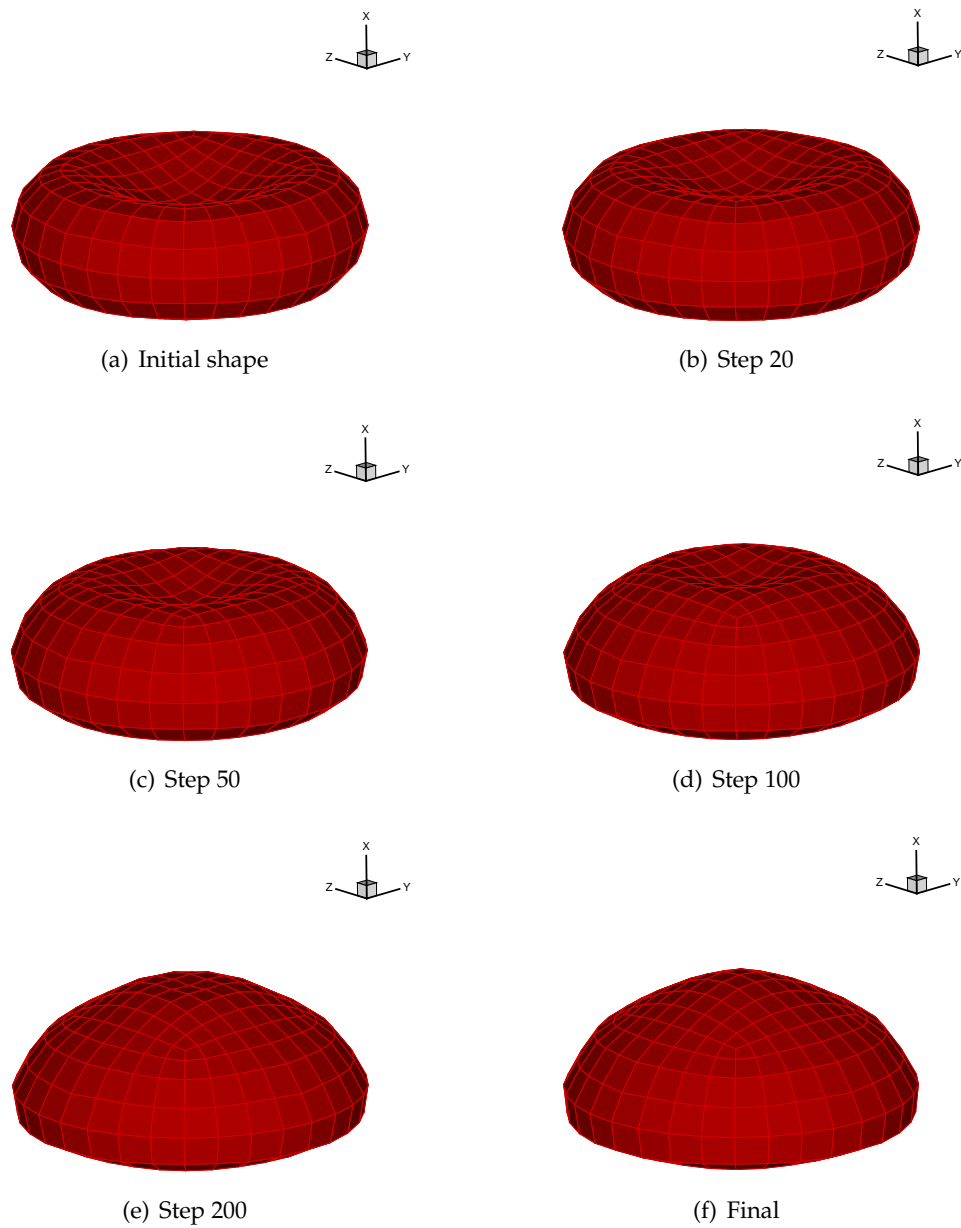


Figure 17: Shape variation of a biconcave cell in a circular cylinder using a membrane forces model.

bending forces model. It can be seen that the cell deformation can be much smaller to bear the external load applied by the surrounding fluids due to the bending stiffness. Again, the bending stiffness of a cell membrane can play a significant role in cell motion simulation.

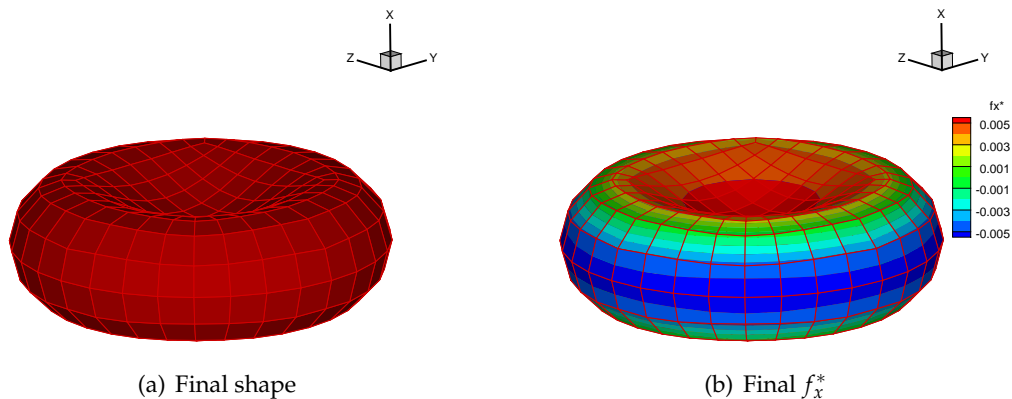


Figure 18: Final results of an initially biconcave cell in a circular cylinder using the present bending forces model.

4 Conclusions

A BEM/FEM coupling approach for simulating the motion of deformable cells in a microfluidic biological fluid flow is presented. The simulation problem can be approximated as the motion of a deformable cell enclosed by a thin elastic membrane with interior and exterior liquids described by the Newtonian low-Reynolds-number hydrodynamics. The biofluid mechanics can be represented by the 3D Stokes flow equations. The low-order BEM model can be developed to solve the velocities and traction forces of the two fluids coupled at the membrane surface efficiently. The FEM model based on a flat thin shell element can be used to predict the membrane load due to the large deformation of a moving cell accurately. Significant improvement in computational efficiency can be achieved due to the one-dimensional reduction in the present BEM and FEM models. The BEM solver for the biological fluids can be effectively coupled with the FEM solver for the cell membrane due to the one-to-one coincidence between the BEM panels and the FEM mesh at the membrane surface. The position of the membrane surface nodes can be accurately advanced in time by using the classical fourth-order Runge-Kutta method with a relatively small time step to avoid numerical instability. The present method is applied to the FSI problems of cell motion in a cylindrical flow. The accuracy of the method is verified against the results by Pozrikidis [4]. Furthermore, it is shown that the classical membrane theory will not be applicable if nearly flat local surfaces are developed due to local buckling. Thus, it is important to include the bending stiffness of the cell membrane in order to obtain a more robust model for a stable cell motion simulation.

References

- [1] C. D. Eggleton, A. S. Popel, Large deformation of red blood cell ghosts in a simple shear flow, *Physics of Fluids* 10 (8) (1998) 1834–1845.

- [2] T. W. Secomb, R. Hsu, A. R. Pries, Motion of red blood cells in a capillary with an endothelial surface layer: effect of flow velocity, *American Journal of Physiology - Heart and Circulatory Physiology* 281 (2001) 629–636.
- [3] C. Pozrikidis, Numerical simulation of the flow-induced deformation of red blood cells, *Annals of Biomedical Engineering* 31 (2003) 1194–1205.
- [4] C. Pozrikidis, Numerical simulation of cell motion in tube flow, *Annals of Biomedical Engineering* 33 (2) (2005) 165–178.
- [5] C. Pozrikidis, *Fluid Dynamics - Theory, Computation, and Numerical Simulation*, Kluwer Academic Publishers, Norwell, Massachusetts 02061 USA, 2001.
- [6] C. Zhu, G. Bao, N. Wang, Cell mechanics: Mechanical response, cell adhesion, and molecular deformation, *Annual Review of Biomedical Engineering* 2 (2000) 189–226.
- [7] C. Pozrikidis, Deformed shapes of axisymmetric capsules enclosed by elastic membranes, *Journal of Engineering Mathematics* 45 (2003) 169–182.
- [8] P. R. Zarda, S. Chien, R. Skalak., Interaction of viscous incompressible fluid with an elastic body, in: T. Belytschko, T. L. Geers (Eds.), *Computational Methods for Fluid-Solid Interaction Problems*, American Society of Mechanical Engineers, New York, 1977, pp. 65–82.
- [9] R. Skalak, H. Tözeren, Flow mechanics in the microcirculation, in: J. F. Gross, A. Popel (Eds.), *Mathematics of Microcirculation Phenomena*, Raven Press, New York, 1980, pp. 17–40.
- [10] R. Skalak, N. Özkaya, T. C. Skalak, Biofluid mechanics, *Annual Review of Fluid Mechanics* 21 (1989) 167–204.
- [11] M. Dao, C. Lim, S. Suresh, Mechanics of the human red blood cell deformed by optical tweezers, *Journal of the Mechanics and Physics of Solids* 5 (2003) 2259–2280.
- [12] F. Feng, W. S. Klug, Finite element modeling of lipid bilayer membranes, *Journal of Computational Physics* 220 (2006) 394–408.
- [13] D. Boal, *Mechanics of the Cell*, Cambridge University Press, Cambridge, 1992.
- [14] J. Li, M. Dao, C. T. Lim, S. Sureshy, Spectrin-level modeling of the cytoskeleton and optical tweezers stretching of the erythrocyte, *Biophysical Journal* 88 (2005) 3707–3719.
- [15] C. Lim, E. Zhou, S. Quek, Mechanical models for living cells - a review, *Journal of Biomechanics* 39 (2006) 195–216.
- [16] R. Torii, M. Oshima, T. Kobayashi, K. Takagi, T. E. Tezduyar, Computer modeling of cardiovascular fluid-structure interactions with the deforming-spatial-domain/stabilized space-time formulation, *Computer Methods in Applied Mechanics and Engineering* 195 (2006) 1885–1895.
- [17] H.-J. Bungartz, M. Schafer, *Fluid-structure Interaction: Modeling, Simulation, Optimisation*, Springer-Verlag, Berlin, Germany, 2006.
- [18] W. K. Liu, Y. Liu, D. Farrell, L. Zhang, X. S. Wang, Y. Fukui, Immersed finite element method and its applications to biological systems, *Computer Methods in Applied Mechanics and Engineering* 195 (2006) 1722–1749.
- [19] S. Y. Wang, P. Q. Chen, K. M. Lim, B. C. Khoo, A mass conservative coupling approach for fluid-structure interaction simulation of living cells, in: *SMA International Conference 2008 & 5th International Symposium on Nanomanufacturing*, 2008.
- [20] T. W. Secomb, Red blood cell mechanics and capillary blood rheology, *Cell Biophysics* 18 (1992) 231–251.
- [21] T. W. Secomb, Mechanics of red blood cells and blood flow in narrow tubes, in: C. Pozrikidis (Ed.), *Modeling and Simulation of Capsules and Biological Cells*, Chapman & Hall /CRC, Boca Raton, 2003.
- [22] T. Secomb, J. F. Gross, Flow of red blood cells in narrow capillaries: Role of membrane

- tension, *International Journal of Microcirculation: Clinical and Experimental* 2 (1983) 229–240.
- [23] T. W. Secomb, R. Skalak, N. Özkaya, J. F. Gross, Flow of axisymmetric red blood cells in narrow capillaries, *Journal of Fluid Mechanics* 163 (1986) 405–423.
- [24] T. W. Secomb, Flow-dependent rheological properties of blood in capillaries, *Microvascular Research* 34 (1987) 46–58.
- [25] R. Hsu, T. W. Secomb, Motion of nonaxisymmetric red blood cells in cylindrical capillaries, *Journal of Biomechanical Engineering* 111 (1989) 147–151.
- [26] T. W. Secomb, R. Hsu., Analysis of red blood cell motion through cylindrical micropores: Effects of cell properties, *Biophysical Journal* 171 (1996) 1095–1101.
- [27] A. Leyrat-Maurin, D. Barthès-Biesel, Motion of a deformable capsule through a hyperbolic constriction, *Journal of Fluid Mechanics* 279 (1994) 135–163.
- [28] C. Quéguiner, D. Barthès-Biesel, Axisymmetric motion of capsules through cylindrical channels, *Journal of Fluid Mechanics* 348 (1997) 349–376.
- [29] A. Diaz, D. Barthès-Biesel, Entrance of a bioartificial capsule in a pore, *Computer Modeling in Engineering & Sciences* 3 (2002) 321–337.
- [30] H. Zhou, C. Pozrikidis, Deformation of liquid capsules with incompressible interfaces in simple shear flow, *Journal of Fluid Mechanics* 283 (1995) 175–200.
- [31] C. S. Peskin, Numerical analysis of blood flow in the heart, *Journal of Computational Physics* 25 (3) (1977) 220–252.
- [32] S. O. Unverdi, G. Tryggvason, Computations of multi-fluid flows, *Physica D* 60 (1992) 70–83.
- [33] C. Pozrikidis, Computation of stokes flow due to the motion or presence of a particle in a tube, *Journal of Engineering Mathematics* 53 (2005) 1–20.
- [34] C. Pozrikidis, Axisymmetric motion of a file of red blood cells through capillaries, *Physics of Fluids* 17 (2005) 031503–1–031503–14.
- [35] Y.-B. Yang, S.-R. Kuo, *Theory & Analysis of Nonlinear Framed Structures*, Prentice Hall, Singapore, 1994.
- [36] G. K. Batchelor, *An Introduction to Fluid Dynamics*, Cambridge University Press, Cambridge, UK, 2000.
- [37] H. G. Matthies, R. Niekamp, J. Steindorf, Algorithms for strong coupling procedures, *Computer Methods in Applied Mechanics and Engineering* 195 (17–18) (2006) 2028–2049.
- [38] B. Hubner, E. Walhorn, D. Dinkler, A monolithic approach to fluid-structure interaction using space-time finite element, *Computer Methods in Applied Mechanics and Engineering* 193 (2004) 2069–2086.
- [39] A. Legay, J. Chessa, T. Belytschko, An eulerianlagrangian method for fluidstructure interaction based on level sets, *Computer Methods in Applied Mechanics and Engineering* 195 (2006) 2070–2087.
- [40] D. S. Jr, O. von Estorff, W. J. Mansur, Efficient non-linear solidfluid interaction analysis by an iterative bem/fem coupling, *International Journal for Numerical Methods in Engineering* 64 (11) (2005) 1416–1431.
- [41] U. Seifert, Modeling nonlinear red cell elasticity, *Biophysical Journal* 75 (1998) 1141–1142.
- [42] C. T. Lim, M. Dao, S. Suresh, C. H. Sow, K. T. Chew, Large deformation of living cells using laser traps, *Acta Materialia* 52 (2004) 1837–1845.
- [43] T. Belytscho, W. K. Liu, B. Moran, *Nonlinear Finite Elements for Continua and Structures*, John Wiley & Sons Ltd, New York, USA, 2000.
- [44] J. N. Reddy, *An Introduction to Nonlinear Finite Element Analysis*, Oxford University Press, New York, 2004.

- [45] J. H. Ferziger, M. Perit, *Computational Methods for Fluid Dynamics*, 3rd Edition, Springer-Verlag, Berlin, Germany, 2002.
- [46] R. Hine, *The Facts on File Dictionary of Biology*, 3rd Edition, Checkmark Books, New York, 1999.
- [47] P. B. Bareil, Y. Sheng, Y.-Q. Chen, A. Chiou, Calculation of spherical red blood cell deformation in a dual-beam optical stretcher, *Optics Express* 15 (24) (2007) 16029–16034.
- [48] Y. Yawata, *Cell Membrane: The Red Blood Cell as a Model*, Wiley-VCH Verlag, Viernheim, Germany, 2003.
- [49] S. K. Boey, D. H. Boad, D. E. Discher, Simulations of the erythrocyte cytoskeleton at large deformation. i. microscopic models, *Biophysical Journal* 75 (1998) 1573–1583.
- [50] S. Ahmad, B. M. Irons, O. C. Zienkiewicz, Analysis of thick and thin shell structures by curved finite elements, *International Journal for Numerical Methods in Engineering* 2 (1970) 419–451.
- [51] R. H. MacNeal, *Finite Elements: Their Design and Performance*, Vol. 89 of Mechanical Engineering, Marcel Dekker, Inc., New York, 1994.
- [52] O. Ziekiewicz, R. Taylor, *Solid Mechanics*, 5th Edition, Vol. 2 of *The Finite Element Method*, Butterworth-Heinemann, Oxford, UK, 2000.
- [53] Y. W. Kwon, H. Bang, *The finite element method using MATLAB*, 2nd Edition, CRC Press, Boca Raton, 2000.
- [54] Y. X. Zhang, Y. K. Cheung, W. J. Chen, Two refined non-conforming quadrilateral flat shell elements, *International Journal for Numerical Methods in Engineering* 49 (2000) 355–382.
- [55] D. Chapelle, K. J. Bathe, *The Finite Element Analysis of Shells - Fundamentals*, Computational Fluid and Solid Mechanics, Springer, Berlin, Germany, 2003.
- [56] J. Bonet, R. D. Wood, *Nonlinear Continuum Mechanics for Finite Element Analysis*, Cambridge University Press, Cambridge, UK, 1997.
- [57] E. Evans, New membrane concept applied to the analysis of fluid shear- and micropipette-deformed red blood cells, *Biophysical Journal* 13 (9) (1973) 941–954.
- [58] R. Skalak, A. Tözeren, P. R. Zarda, S. Chien, Strain energy function of red blood cell membranes, *Biophysical Journal* 13 (1973) 245–264.
- [59] E. A. Evans, R. Skalak, *Mechanics and Thermodynamics of Biomembranes*, CRC, Boca Raton, 1980.
- [60] C. Pozrikidis, *Modeling and Simulation of Capsules and Biological Cells*, Chapman & Hall/CRC, Boca Raton, 2003.
- [61] D. Chapelle, Reliability of finite element methods for thin shells, in: B. Topping (Ed.), *Computational Mechanics for the Twenty-First Century*, Saxe-Coburg Publications, Edinburgh, UK, 2000, pp. 99–108.
- [62] O. Ziekiewicz, R. Taylor, *The Basis*, 5th Edition, Vol. 1 of *The Finite Element Method*, Butterworth-Heinemann, Oxford, UK, 2000.
- [63] S. S. Rao, *The Finite Element Method in Engineering*, 4th Edition, Elsevier, New York, 2005.
- [64] E. Hinton, D. R. J. Owen., *Finite element software for plates and shells*, Pineridge Press, Swansea, U.K., 1984.
- [65] D. Braess, *Finite elements: Theory, fast solvers, and applications in solid mechanics*, 2nd Edition, Cambridge University Press, Cambridge, UK, 2001.
- [66] C. A. Felippa, B. Haugen, A unified formulation of small-strain corotational finite elements: I. theory, *Computer Methods in Applied Mechanics and Engineering* 194 (2005) 2285–2335.
- [67] J. Argyris, An excursion into large rotations, *Computer Methods in Applied Mechanics and Engineering* 32 (1982) 85–155.

- [68] R. A. Spurrier, A comment on "singularity-free extraction of a quaternion from a direction cosine matrix", *Journal of Spacecraft and Rockets* 15 (1978) 255.
- [69] L. C. Wrobel, M. H. Aliabadi, *Applications in Thermo-Fluids and Acoustics*, Vol. 1 of *The Boundary Element Method*, John Wiley & Sons, New Jersey, 2002.
- [70] C.-H. Lee, J. N. Newman, Computation of wave effects using the panel method, in: S. Chakrabarti (Ed.), *Numerical models in fluid-structure interaction*, WIT Press, Southampton, UK, 2005, Ch. 6.
- [71] Y. Saad, M. Schultz, GMRES - a generalized minimal residual algorithm for solving non-symmetric linear-systems, *SIAM Journal on Scientific and Statistical Computing* 7 (3) (1986) 856-869.
- [72] J. R. Phillips, J. K. White, A precorrected-FFT method for electrostatic analysis of complicated 3-d structures, *IEEE Transaction on Computer-Aided Design* 16 (10) (1997) 1059-1072.
- [73] L. Greengard, V. Rokhlin, A fast algorithm for particle simulations, *Journal of Computational Physics* 73 (1987) 325-348.
- [74] K. J. Bathe, E. N. Dvorkin, A formulation of general shell elements - the use of mixed interpolation of tensorial components, *International Journal for Numerical Methods in Engineering* 22 (3) (1986) 697-722.
- [75] J. E. Akin, *Finite Element Analysis with Error Estimators*, Elsevier Butterworth-Heinemann, Burlington, MA, 2005.
- [76] W. McGuire, R. H. Gallagher, R. D. Ziemian, *Matrix Structural Analysis*, 2nd Edition, John Wiley & Sons, Inc., New York, USA, 2000.